CEAS Aeronautical Journal
https://doi.org/10.1007/s13272-024-00790-2

ORIGINAL PAPER

Acoustic and aerodynamic evaluation of DLR small-scale rotor configurations within GARTEUR AG26

J. Yin[1] · F. De Gregorio[2] · K.-S. Rossignol[1] · L. Rottmann[1] · G. Ceglia[2] · G. Reboul[3] · G. Barakos[4] · G. Qiao[4] · M. Muth[5] · M. Kessler[5] · A. Visingardi[2] · M. Barbarino[2] · F. Petrosino[2] · A. Zanotti[6] · N. Oberti[6] · A. Savino[6] · G. Bernardini[7] · C. Poggi[7] · L. Abergo[6] · F. Caccia[6] · A. Guardone[6] · C. Testa[8] · S. Zaghi[9]

Received: 2 June 2024 / Revised: 30 September 2024 / Accepted: 28 October 2024

Abstract
This paper presents the activities performed in the GARTEUR Action Group HC/AG-26 to study the acoustic and aerodynamic characteristics of small rotor configurations, including the influence of the rotor-rotor interactions. This paper will focus on comparisons between numerical activities and wind tunnel results on a small rotor provided by DLR. The wind tunnel models included a Rotor/Rotor/Pylon in isolated, tandem and coaxial configuration. The wind tunnel experiments for acoustics were performed in DLR's Acoustic Wind Tunnel Braunschweig (AWB) and PIV test were performed in CIRA within a joint CIRA/DLR test program. For simulations, the numerical approaches from each partner are applied. The aerodynamic simulations necessary for the aeroacoustic predictions are conducted with various fidelity numerical methods, varying from lifting line to CFD. The acoustic values on the microphone positions are evaluated using Ffowcs Williams/Hawking (FW-H) formulation by all partners. The acoustic and aerodynamic predictions are compared to test data, including performance, PIV and acoustic directivity.

Keywords Small rotor-rotor configuration · Rotor/propeller noise · Acoustic wind tunnel · PIV · Numerical approaches · Free wake · CFD · GARTEUR

Abbreviations

D	Rotor diameter (0.33 m)
f	Frequency (Hz)
p0	Air pressure in an undisturbed medium, Pa
rev	Revolution
T	Thrust in N
AWB	Acoustic Wind tunnel in Braunschweig
BPF	Blade Passing Frequency, Hz
FW-H	Ffowcs Williams/Hawkings acoustic analogy
LHR	Left-handed rotor
OASPL	Overall sound pressure level, dB
PIV	Particle Image Velocimetry
R	Rotor radius (0.165 m)
RHR	Right-handed rotor
ROI	Region of Interest
RPM	Rotor revolution per minute
SPL	Sound pressure level, dB

✉ J. Yin
jianping.yin@dlr.de

[1] German Aerospace Center-DLR, Braunschweig, Germany

[2] Italian Aerospace Research Center-CIRA, Capua, Italy

[3] DAAA, ONERA, Institut Polytechnique de Paris, Châtillon, Paris, France

[4] University of Glasgow, Glasgow, Scotland, UK

[5] University of Stuttgart, Stuttgart, Germany

[6] Politecnico di Milano - Dipartimento di Scienze e Tecnologie Aerospaziali, Milan, Italy

[7] Roma Tre University, Rome, Italy

[8] CNR-INM, Rome, Italy

[9] CNR-IAC, Rome, Italy

1 Introduction

Multirotor systems are increasingly applied to Vertical Take-Off and Landing (VTOL) configurations. Multirotor systems are popular for small-scale drones used for surveillance, monitoring, search, aerial surveying and photography, among other applications. In the context of a growing interest in developing urban air mobility (UAM) solutions and providing answers to fundamental questions regarding

Published online: 23 November 2024

the aerodynamic and acoustic characteristics of these new vehicles, the GARTEUR Action Group HC/AG-26 [1] has been established. There are 14 partners involved in the group activities coordinated by DLR. The objectives of this AG are (1) to gain knowledge in noise generation and noise propagation of multirotor systems under the influence of the installation effects and (2) to develop and validate numerical prediction methods for the noise prediction for multirotor systems. For the code validations, the results obtained by each partner were shared among the action group. Three data bases of test data were available from DLR [2, 3], CIRA/CUSANO [4, 5] and PoliMi [6]. In addition, the first common test campaigns involving Particle Image Velocimetry (PIV) measurement were carried out by CIRA/DLR [7], using the DLR small rotor configurations [2, 3]. The common experiment aims at using the dedicated capabilities of the partner's wind tunnels to improve the validation database for the simulations and at the same time to validate the experimental accuracy by repeating the same experiments in several wind tunnels.

This paper will focus on the numerical comparison activities with the wind tunnel results involving only DLR small rotor configurations, including isolated and rotor/rotor configurations. For the simulation of the various test cases, the numerical approaches from each partner are applied. The aerodynamic simulations necessary for the aeroacoustic predictions are conducted with various fidelity numerical methods, varying from lifting line to CFD. In the case of the acoustic installation effects, a scattering code can be applied or directly extract from CFD. The introduction of the experimental approach used in the acoustic/PIV test, including the rotor model, the instrumentation and the data reduction are also presented. The methodologies applied in the numerical simulations by the partners are then described and analyzed to point out their strengths and weaknesses. The aerodynamic and acoustic predictions are analyzed and compared either code to code or with available test results for the different configurations considered. The aerodynamic results are presented in terms of the aerodynamic performance and ensemble average velocity fields. The acoustic results are presented in terms of sound pressure level (SPL) directivities, spectra and sound pressure time histories.

2 Description on the acoustic and PIV test setup

2.1 Acoustic test setup and measurement in DLR AWB

The Acoustic Wind tunnel in Braunschweig (AWB) [8] is DLR's small-scale high-quality anechoic testing facility. It is an open-jet Göttingen-type wind tunnel capable of running at speeds of up to 65 m/s and optimized for noise measurements at frequencies above 250 Hz. The nozzle is 1.2 m high by 0.8 m in width. A special rig was designed to extend the capabilities of the facility to meet the requirements of simultaneous measurements of multiple rotors under static and flight conditions, e.g., Figs. 1 and 2. The rotor was supported by a central pylon fitted with a streamlined fairing limiting interference with the slipstream. The only eventual potential field should happen in hover by the pylon is very thin the vertical direction so it is not likely. The motor is located outside the pylon (Fig. 3) to avoid the overheating problem. All load cells are inside the pylon to isolate from the motors to minimize the impact of temperature changes and electromagnetic fields from the motors on measurements.

Fig. 1 Experimental setup: single rotor (left), coaxial rotors (middle) and tandem rotors (right)

The main objective of the selected mechanical design is to enable the investigation of the effect of flow and shaft angle on the acoustic radiation of a broad range of propeller configurations; isolated, coaxial, tandem with vertical and lateral offset, e.g., Fig. 1. The dimensions of the AWB test section, allow the investigations of rotors with a diameter of up to approximately 0.4 m. The rig is designed to allow shaft angle variations in the range $\alpha \pm 30°$ and testing at free-stream velocities up to $U_\infty \approx 30$m/s.

Above $U_\infty \approx 30$m/s, rig vibrations will have a noticeable influence on the loads, moments and acoustic measurements. Furthermore, the rig allows for lateral spacing settings in the range $\Delta y \pm 0.15$m, streamwise spacing settings in the range $\Delta x \pm 0.3$m and vertical spacing settings in the range $\Delta z \pm 0.3$m. These setting values are valid for the current set of propellers considered herein. The whole structure of the rig is based on standard X-95 rails and carriers. This choice allows for easy changes in configuration. The rig is fixed to a rotating axle at its central point, i.e., on the left-hand side of Fig. 2 to allow variations in rotor shaft angle.

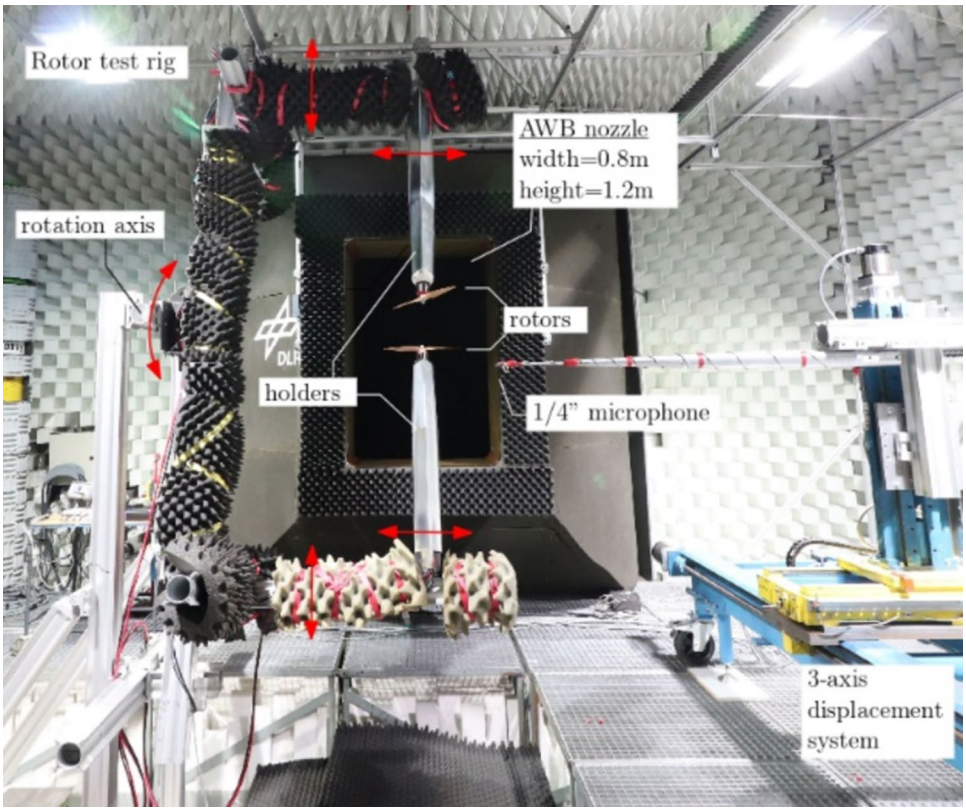

Fig. 2 Overview of the full test rig and microphone setup installed in the AWB's test section. Center: coaxial configuration

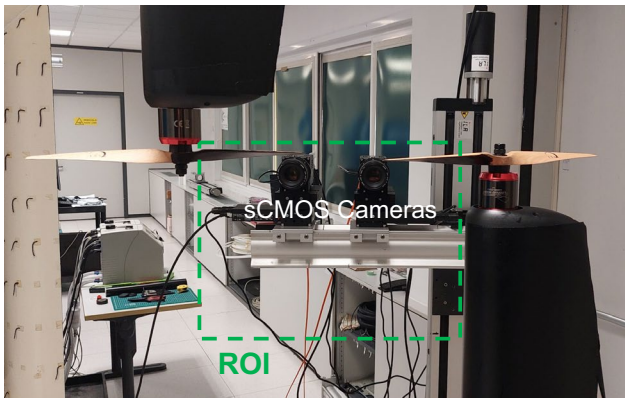

Fig. 3 PIV set-up for tandem case in CIRA

2.2 PIV test setup and measurement in CIRA

To characterize interactions in the flow field, isolated and multiple rotor configurations have been investigated in CIRA/DLR common tests, by means of standard two and three-component PIV-measurement techniques. Several configurations have been investigated at $\Omega = 8025$, 10,120 and 12,000 rotor revolution per minute (RPM), respectively. Two propellers were investigated in tandem configuration by two sCMOS double-frame cameras, characterized by 5.5 Mpx and 16bit pixels dynamic range. The cameras were equipped with 50 mm Canon EF focal lenses, and mounted on motorized rotating motors, allowing for camera rotation and Scheimplugh correction.

The two cameras were installed side-by-side and horizontally oriented as shown in Fig. 3, to increase the sizes of the measured region.

The measurement region was illuminated by a double-head Nd-Yag laser with a pulse energy of 150 mJ at a wavelength of 532 nm and a repetition rate of 10 Hz.

The flow measurements provide a vector pitch of $\Delta x = 1.41mm$. The error of the PIV cross–correlation procedure is evaluated as 0.1 px as the first estimation (Raffel et al. [9]). Using the current values for the optical resolution (11.3 px/mm) and the laser double–pulse delay (25–35 µs), this provides a velocity error of ΔV of ~ 0.25 m/s to 0.35 m/s. For a detailed description of the PIV-measurement system, the reader is referred to the work of De Gregorio et al. [7].

For the tandem configuration, the measured region covers between $-2.13 < x/R < 0.29$ along the radial direction and the area from slightly above the propeller disk until down to little more than two radii distance $z/R = -2.1$ (Figs. 3, 5a). For the coaxial configuration, a different camera setup was adopted considering the presence of the fairing below the propeller blade. The PIV cameras were vertically mounted side-by-side (Fig. 4) assuring a measurement region ranging

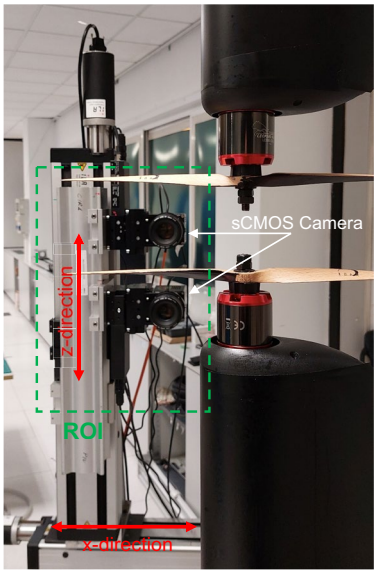

Fig. 4 PIV set-up for coaxial configuration in CIRA

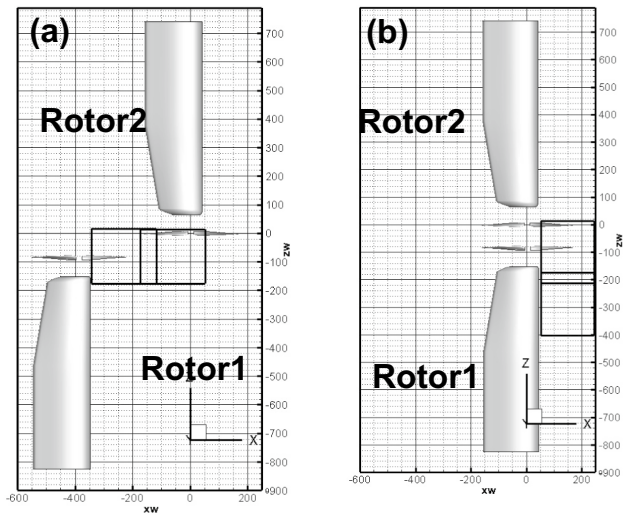

Tandem Δx=1.18 D and Δz=0.25 D

Coaxial: Δx=0 D and Δz=0.25 D

Fig. 5 PIV set-up for two rotor case in CIRA

along the x-axis between $0.16 < x/R < 1.3$ and toward the z-axis down to $z/R = -2.16$ (Fig. 5b).

2.3 Rotor and pylon

The rotor is a commercially available one (Xoar model PJN). For this paper, the test results from a two-blade 13 × 7 rotor including a rotor support (pylon), as shown in Fig. 6 are chosen for validating the numerical simulations. The rotor 13 × 7 represents a rotor with 13 inches or 0.33 m in diameter and 7 inches in pitch. The rotor, pylon planform and the form of the section profiles are presented in Fig. 6. The twist (θ), thickness (t) and chord(c) distribution given in Fig. 7 were derived according to a scanned surface.

The rotors are mounted on Leopard LC5065 motors coupled to YGE 205HVT speed controllers and SM300-Series 3300 W DC power supplies. This combination allows RPM up to 13,000 to be reached. For each rotor, performance data, in terms of thrust and torque, is acquired through miniature six-components load cells, Modell K6D40 from ME-Meßsysteme GmbH, mounted directly underneath the propellers. Each rotor RPM is acquired through a 1/rev-signal generated by a Hall-effect sensor mounted to the rotor's shaft. This signal also serves as a trigger signal for data post-processing. Two multi-rotor configurations will be considered. An overview of these is given in Fig. 5a and b. The so-named tandem configuration is defined by a relative position between the two rotor axes of $\Delta x = 1.18$ of the rotor diameter D, $\Delta y = 0$ and a vertical distance of $\Delta z = 0.25D$. The coaxial configuration has Δx and Δy null, while the axial distance between the propeller disks is equal to $\Delta z = 0.25$ D. For the isolated rotor configuration, the rotor is a right-handed rotor (RHR) and rotates counter-clockwise. For the multirotor configurations, the lower rotor is the RHR which is same as the isolated one while the upper rotor is a left-handed rotor (LHR) and rotates clockwise.

3 Description of methodologies applied in the numerical simulations by the partners

The numerical investigations are performed by each partner applying either in-house-developed or commercial computational tools. The aerodynamic simulations necessary for the aeroacoustic predictions are conducted with a range of different fidelity numerical methods, varying from lifting line to CFD.

3.1 CIRA

The CIRA aerodynamic simulations were carried out using the medium-fidelity code RAMSYS [10], which is an unsteady, inviscid and incompressible free-wake vortex lattice boundary element methodology (BEM) solver for multi-rotor, multi-body configurations developed at CIRA. It is based on Morino's boundary integral formulation [11] for the solution of Laplace's equation for the velocity potential φ. The surface pressure distributions are evaluated by applying the unsteady version of Bernoulli equation, which is then integrated to provide the forces and moments on the configuration and the surrounding obstacles. A computational

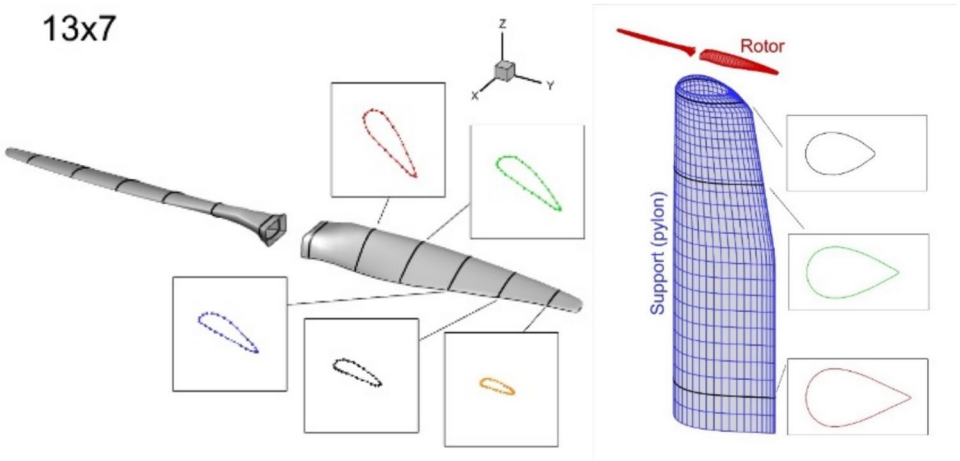

Fig. 6 Rotor and pylon model

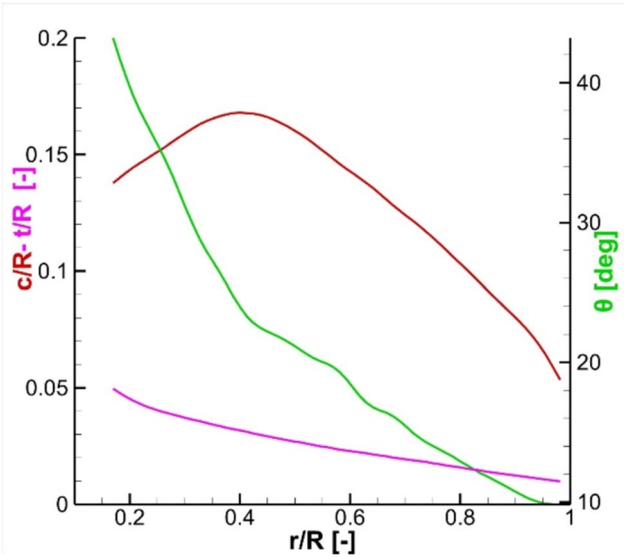

Fig. 7 The twist (θ), thickness (t) and chord (c) distribution

acceleration is obtained by applying the module for symmetrical flows and geometries implemented in the solver and the parallel execution via the OpenMP API.

The ACO-FWH solver is used for computing the acoustic free-field generated by the rotor blades. It is based on the Ffowcs Williams/Hawkings (FW-H) formulation [12] described in [13–15]. The advanced time formulation of Farassat 1A is employed, and the linear terms (the so-called thickness and loading noise contributions) are computed through integrals on the moving blades' surface (impermeable/rigid surface formulation). The computational acceleration is obtained by a parallel execution via the MPI API. The simulation of the aeroacoustic free-field was carried out using the aerodynamic database evaluated by RAMSYS, and consisting of the rotor blade-pressure distributions.

3.2 DLR

The free-wake panel method UPM [3, 16, 17] is based on a velocity-based, indirect potential formulation using a combination of source and vortex distribution on the solid surfaces and vortex panels in the wake. Compressibility effect of the flow are considered by applying the Prandtl–Glauert correction. The blade vortex interaction (BVI) is captured thanks to the free-wake model used in UPM. Depending on the configurations, all interactions among rotors, rotor, pylon are considered. The validation effort is supported by CFD TAU steady simulations on selected hover test cases. The unstructured CFD code TAU is based on the solution of the Reynolds averaged Navier–Stokes equations on hybrid unstructured meshes. The solver uses a cell vertex scheme to discretize the mass, momentum and energy fluxes [18]. In the current paper, the 2nd-order accuracy central scheme was used for spatial discretization. Scalar dissipation has been used as the central dissipation scheme. The simulation is steady. The temporal discretization is solved with a multistep Runge–Kutta scheme and is independent of time due to the local time step method. The propeller is simulated in the rotating reference frame, wherein the flow is assumed to be steady. The two-equation turbulence model Menter SST was used. Furthermore, all surfaces were simulated fully turbulent.

The Aeroacoustic Prediction System based on an Integral Method, APSIM [19], is designed to calculate wave propagation over large distances in uniform flows. The methodology is based on FW-H formulation [12] and only linear sound propagation is considered. In general, the aeroacoustic computation into the far field is split into two steps for current applications: In a first step the pressure data on the rotor is computed by aerodynamic codes and provided to APSIM; in a second step the sound propagation into the far field is calculated with APSIM. Validations of UPM, TAU and APSIM were intensively conducted during various projects.

3.3 ONERA

The aerodynamic simulations performed by ONERA are realized with the PUMA code [21]. PUMA (potential unsteady methods for aerodynamics) is an unsteady lifting line / free-wake solver developed at ONERA since 2013. It is built on a coupling between an aerodynamic module and a kinematic module. The aerodynamic module relies on a lifting line method with a free-wake model using the Mudry theory [20], which describes the unsteady evolution of a wake modelled by a potential discontinuity surface. The lifting line method relies on two-dimensional airfoils characteristics through lookup tables computed preliminary by CFD with the ONERA elsA1[1] code [22]. Some blade sweep correction and dynamic stall models are added. Concerning the kinematic module, it is based on a rigid multi-body system approach using a tree-like structure with links and articulations. It enables any arbitrary motion between the different elements. To speed up the computation the code has been parallelized using OpenMP and the Multilevel Fast Multipole Method has been implemented.

Concerning the numerical parameters used for the computations, they are based on previous experience. The lifting line is divided in 30 radial stations using a square root distribution. A time step of 5° was used over 25 rotor revolutions over which the last 6 are used for post-processing. The computations do not account for the rotor hub or other test rig components.

The unsteady spanwise distribution of loads obtained with PUMA are used as input for the KIM code [23, 24] to determine the noise emission of the rotor thanks to a FW-H formulation implemented in a non-compact advanced time approach. Since, only sectional forces are available and in order not to consider noise sources compacted in the chord direction, the surface pressure is reconstructed over the entire blade thanks to interpolation based on the pressure distributions computed and stored during the airfoil polar computations.

3.4 PoliMi

The single propeller case was simulated with a mid-fidelity and a high-fidelity aerodynamics solver, respectively DUST and SU2, while dual propellers configurations were simulated with DUST only. DUST is an open-source software developed by Polimi to simulate the interactional aerodynamics of unconventional rotorcraft configurations. The code, released as free software under the open-source MIT license, relies on an integral boundary element formulation of the aerodynamic problem and a vortex particle model of the wakes [25]. SU2 is an open-source toolkit distributed by the SU2 Foundation [26], freely available and licensed under the GNU Lesser General Public License. It uses the finite volume approach to solve partial differential equations (PDE) on unstructured meshes. It solves the Unsteady Reynold-averaged Navier-Stoke (URANS) equations to analyze typical aeronautical problems that involve turbulent flows in the compressible regime. For SU2 simulations blades were discretized using 130 cells in radial direction and 125 cells in chordwise direction. The first surface cells satisfy $y+ < 1$ and an extrusion up to 70 cells with 1.1 growth rate was used to build up the boundary layer around the blade. The total amount of the cells used to build the rotor mesh was 15 million while the total mesh grid was made by 30 million cells. The temporal discretisation used in the URANS simulations was 1 deg/iter while 3 deg/iter was used for DUST simulations. Aerodynamic results obtained with both solvers are not trimmed. The aeroacoustic signature is computed by solving Ffowcs Williams-Hawkings [12] (FWH) equations. The surface pressure field on the propeller computed with the two solvers is provided as input to the same acoustic module [27]. The pylon for both DUST/SU2 simulations is not modeled.

3.5 Roma Tre University/CNR

Under the framework of GARTEUR AG-26, Roma Tre University (RM3) and the National Research Council of Italy (CNR) are collaborating to advance their collective understanding of drone aeroacoustics. Aerodynamic and aeroacoustic solvers used by both research units are based on tools developed over the past twenty years, which have been extensively validated on helicopter and tiltrotor configurations [28, 29], marine/aeronautical configurations powered by rotating wings [30–32] and wind turbine applications [33]. For simplicity, all results presented in this paper are labeled as RM3. The aerodynamic module is based on the boundary integral formulation for the velocity potential presented in [34], suited for helicopter configurations where blade–vortex interaction (BVI) occurs. This formulation is fully 3D, can be applied to bodies with arbitrary shape and motion, and allows the calculation of both wake distortion and blade-pressure field. It assumes the potential field to be divided into an incident field, generated by doublets over the wake portion not in contact with the trailing edge (far wake), and a scattered field, generated by sources and doublets over the body and doublets over the wake portion very close to the trailing edge (near wake). This procedure allows one to overcome the numerical instabilities arising when the wake, modeled as a surface of doublets, comes too close to or impinges on the body. Recalling the equivalence between the surface distribution of doublets and vortices, the contribution of the wake portion experiencing BVI (far

[1] *elsA V4.2.01 Airbus-Safran-ONERA property.*

Table 1 Main characteristics of the codes used by the partners

Partner	Code	Description
CIRA	RAMSYS, ACO-suite	Unsteady, inviscid and incompressible free-wake Boundary Element Method (BEM), Ffowcs Williams /Hawkings (FW-H)
DLR	UPM, TAU APSIM	Free Wake Panel method, unstructured CFD, FW-H
ONERA	PUMA, KIM	Unsteady lifting line/free-wake solver, FW-H
PoliMi	DUST, SU2	Free Wake Panel method and unsteady, compressible (URANS) CFD, FW-H
ROMA3/CNR	RM3	Free wake boundary element method (BEM) + FWH
Uni Stuttgart	FLOWer, ACCO	Flower: unsteady, compressible (URANS) CFD solver with Chimera technique, FW-H Solver with source-time dominant algorithm
UoG	HMB3-HFWH	HM3 CFD solver, FW-H coupled with HMB3

Table 2 Summary of the numerical resolution for mid-fidelity aerodynamic tool used by the partners

Partner	Panel per blade	Panel per pylon	Time step ISO/Multi	Num. of revs ISO/Multi
DLR UPM	1624	1470	5°/2°	16/8
CIRA RAMSYS	1450	1392	2°/2°	9/9
ONERA PUMA	N.A	No pylon	5°/5°	25/25
PoliMi DUST	1050	No pylon	3°/3°	15/15
ROMA3/CNR RM3	3150	No pylon	3°/3°	20/20

wake) is expressed in terms of thick vortex (i.e., Rankine vortices) distributions. The shape of the wake can be either assigned (prescribed-wake analysis) or obtained as a part of the solution (free-wake analysis) by a time-marching integration scheme in which the wake is moved accordingly to the velocity field computed from the potential solution. Once the potential field is known, the Bernoulli theorem yields the pressure distribution on the body that, in turn, is used both to determine the aerodynamic loads and as an input to the aeroacoustic solver to predict the radiated noise.

The aeroacoustic analysis is performed by a prediction tool based on the FWH equation [12]. The solution of the FWH equation is achieved through the boundary integral representation known as the Farassat Formulation 1A [35].

3.6 Uni Stuttgart (IAG)

For high-fidelity simulations, a framework consisting of FLOWer and ACCO was used at the Institute of Aerodynamics and Gas Dynamics (IAG) at the University of Stuttgart. CFD results are obtained with the block-structured code FLOWer, originally developed by DLR [36] and continuously extended at the IAG for rotorcraft and multirotor applications [37]. Acoustic coupling was provided by IAG's FW-H solver ACCO [38] which uses the transient flow data provided by FLOWer as an input.

FLOWer solves the three-dimensional, compressible RANS equations and enables unsteady flow solutions (URANS). The discretization of time and space is applied separately by the method of lines. For temporal discretization a 2nd-order dual time stepping is used [39] with a time step of 0.5° to resolve acoustic waves, while for spatial discretization a 5th-high-order weighted essentially non-oscillatory (WENO) scheme by Borges [40] is used. Furthermore, the k-omega turbulence model was applied to close the URANS equations. Using the Chimera technique separate meshes were created for the background and rotor, utilizing hanging grid nodes to reduce the numerical expense. The

Table 3 Summary of CFD grids and attributes used by the partners

Partner	Grid cells rotor (million)	Grid cells total ISO/multi (million)	Time step ISO/multi	Num. of revs ISO/multi	Temporal/spatial discretization	Turbulence model
DLR TAU	NA	34.2	stationary	stationary	–/2nd order	Menter SST
IAG FLOWer	6.6	14.3/24	0.5°/0.5°	25/25	2nd/5th order	k-omega
PoliMi SU2	15	30	1°/1°	20/20	2nd/2nd order	k-omega
UoG HMB3	4.7	18.3	1°/2°	20/20	3rg/3rd order	Menter SST

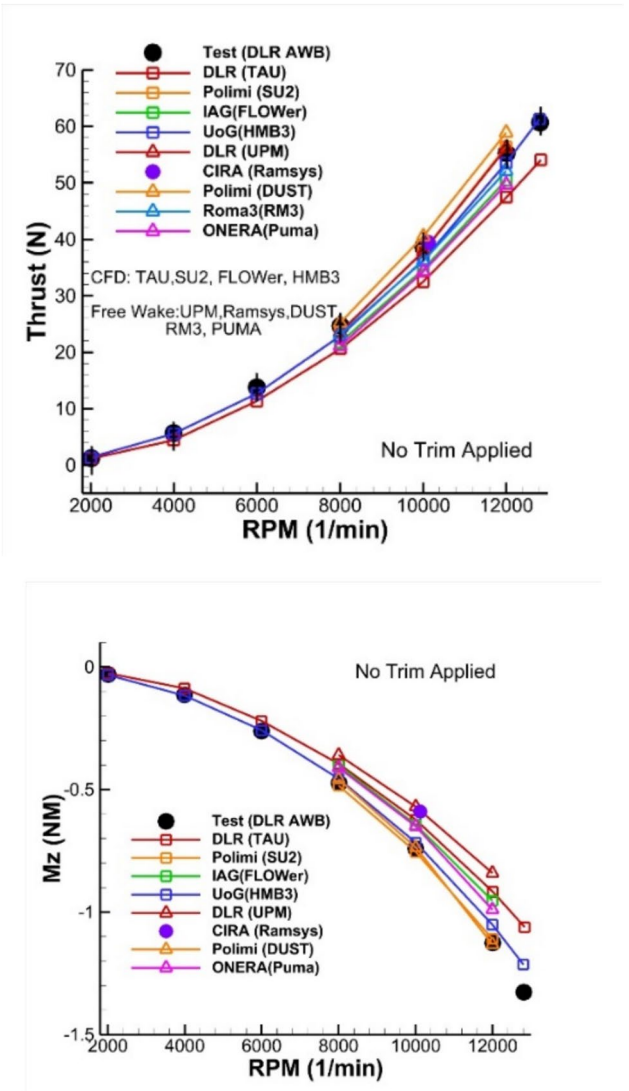

Fig. 8 Time averaged rotor thrust and torque for 8000, 10,000 and 12,000 RPM

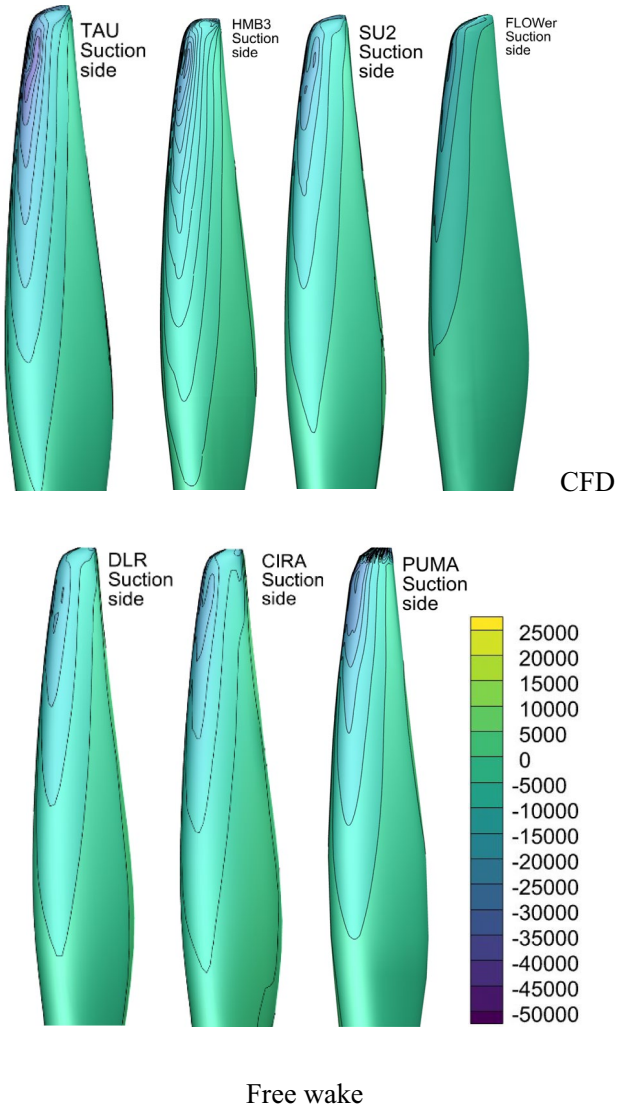

Fig. 9 Suction and pressure side distribution of the instantaneous p-p0 at rpm 10,000

spatial resolution of a single rotor was achieved by 6.6 million cells. The rotor surface was meshed with 144 cells in radial and 80 cells in chordwise direction with a refinement toward the blade tip, leading edge and trailing edge with cell sizes of less than one thousandth of the radius. The rotor mesh is extruded in wall normal direction with 52 cells. The first surface cells satisfy $y+ < 1$ and an extrusion up to cell sizes corresponding 10% of the chord length is applied. The spatial discretization in the background mesh was based on the resolution of the first harmonic wave length, with 15 cells discretizing the wave length of the Blade Passing Frequency (BPF).

The acoustic code ACCO is an in-house code of the IAG, which uses an acoustic integration surface for the generation of sound emissions. For the integration either the physical surfaces or a permeable surface surrounding the object of interest can be used. For the performed simulations, the physical blade data of 4 full rotor revolutions are used and the CFD input data treated as periodic. The integration is achieved through the physical surface of the rotor blade, which includes all tonal sound sources. In addition, a 6th-order filter with 100 filter runs to reduce the higher oscillations found due to separation on the rotor blade. The studies indicated that the filter did not change the frequency contents up to 7.5 kHz.

3.7 UoG (University of Glasgow, Glasgow)

Helicopter Multi-Block (HMB3) code is employed in this study. The solver can accurately predict the aerodynamic

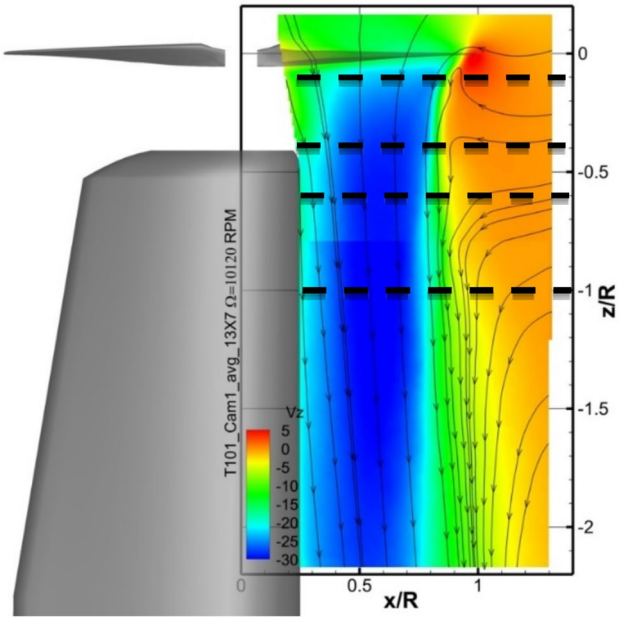

Fig. 10 Iso-contours with streamtraces of the ensemble-average flow field color-coded with the velocity vertical component at at Ω = 10,120 RPM

performance, acoustics of propagation, and has been widely used in the investigation of rotorcraft flows [41, 43], helicopter rotor aeroelasticity [44, 51], and missile trajectory prediction [45]. Moreover, a good agreement when compared to experimental results in aerodynamics, acoustics and aeroelasticity of propellers, can be seen in a previous study [46, 50]. Most recently, its ability to capture the interactions of multi-rotor flows and ducted propeller flows was documented [47]. HMB3 solves the Unsteady Reynolds Averaged Navier–Stokes (URANS) equation in integral form using the Arbitrary Lagrangian–Eulerian formulation for time-dependent domains, including moving boundary layers. HMB3 uses a cell-centered finite volume approach to discrete Navier–Stokes equations on multi-block, structured grids. The 3rd-order MUSCL (Monotone Upstream-cantered Schemes for Conservation Laws) approach is applied to provide high-order accuracy in space. In the present work, simulations are performed with the $k-\omega$ shear stress transport (SST) [48] turbulence model.

The computational grids used for propellers have a typical C-H topology. The spacing distribution has been set to the condition $y^+ \leq 1$, resulting in a first cell size normal to the surfaces of approximately 1.0×10^{-5} c as tested a-posteriori.

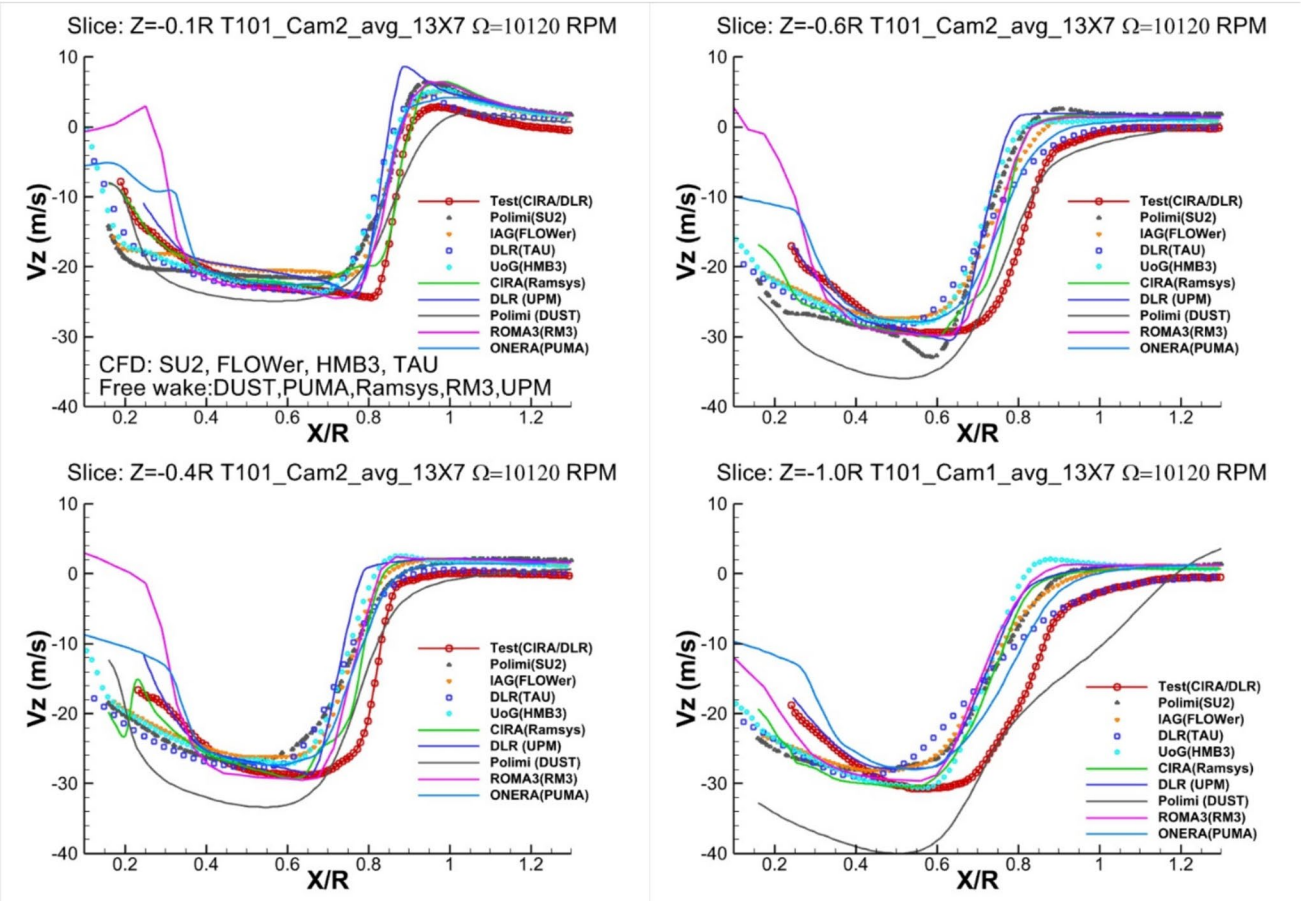

Fig. 11 Vertical velocity trend along radial distance at Ω = 10,120 RPM for different z-stations

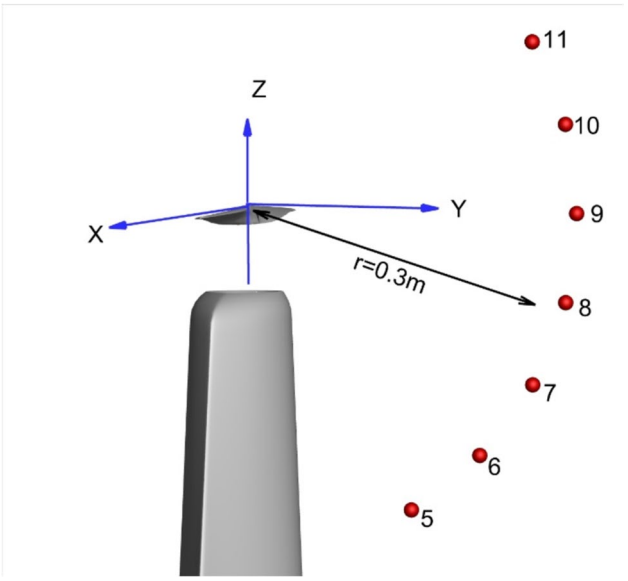

Fig. 12 Microphone positions for the isolated rotor case

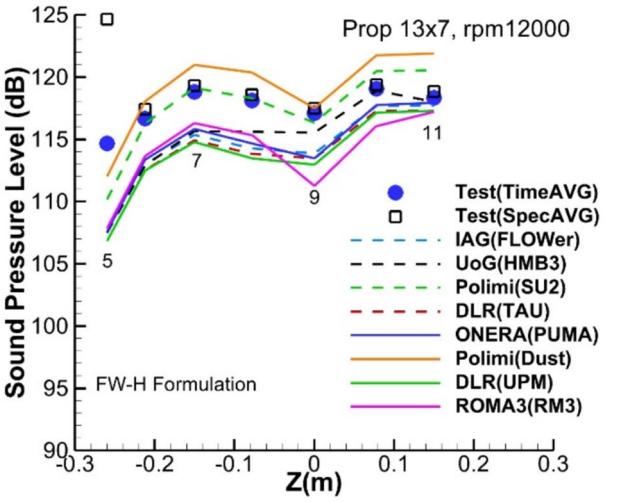

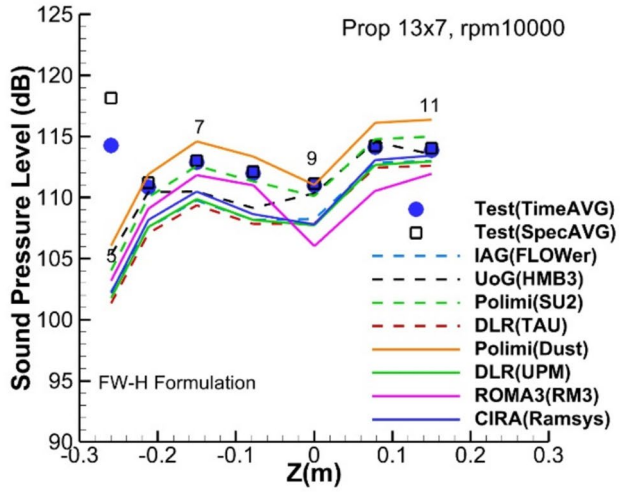

Fig. 13 OASPL polar directivity taken from Mic 5 to Mic 11 for RPM 12000 and 10,000

Adiabatic, non-slip, wall boundary conditions were applied at rotors. The spatial resolution was achieved with 175 cells in the radial direction, 275 cells around each blade section in the circular direction and 41 cells in the wall normal direction. The refined regions were near the blade leading, trailing edges and tip region. The temporal resolution from the unsteady computations used a time step corresponding to 2° of rotor rotation. This was the same for all cases. The convergence of the implicit scheme was determined based on the reduction of the flow-field residual, compared to the previous time step. Either a three-order-of-magnitude reduction or 300 inner iterations, was considered sufficient for each unsteady step. For isolated rotors and propellers in axial flight, the azimuthal symmetry of the configuration can be exploited, whereby only a fraction of the grid needs to be generated. The Rotating Reference Frame (RRF) method is implemented in HMB3 [42] for simulations with rotational periodicity. The governing flow equations are reformulated and solved in a non-inertial reference frame, thus transforming the unsteady problem into a steady one.

Regarding acoustics, the present work estimates the near-field information derived from pressure fields computed with the high-fidelity HMB3 tool. The sound pressure signal was obtained by subtracting the time-averaged pressure from the time-dependent data. All CFD grids were designed to have at least 20 cells in the near-field region to capture the target wavelength, which is calculated based on 20 times the Blade Passing Frequency (BPF = 400 Hz) [50]. The coupling of HMB3-HFWH tools was applied with the input of surface pressure fields computed by HMB3 to efficiently calculate the far-field acoustics. Current work focuses on the non-porous formulation with a completely anechoic condition. Extensive code-to-code comparisons of the current acoustic solver have been validated by by Smith [49].

3.8 Summary

The numerical methodologies used in the group are summarized in Table 1.

For a mid-fidelity aerodynamic tool based on potential formulation and free wake, the specific number of panels on the blade and pylon utilized in this paper is listed in Table 2. The summary of CFD grids utilities and some attributes are given in Table 3. The numbers are derived according to the convergence of the code results.

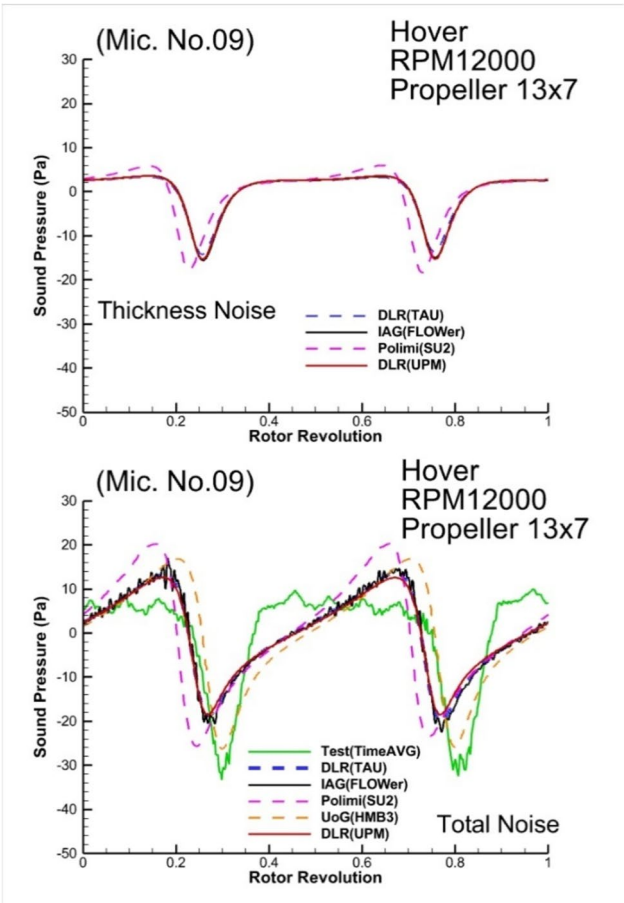

Fig. 14 Time histories at Mic. position 9 for RPM 12000. Up: thickness noise; Low:total noise

4 4 Results for the isolated rotor

4.1 Hover at RPM = 8000, 10,000, 12,000

4.1.1 Aerodynamic performance

A comparison of the measured and simulated time-averaged rotor thrust and torque is given in Fig. 8. No trim is applied in all simulations. Figure 8 indicates that general tendencies captured in the measurements are reproducible using all computational tools. The differences from the test results are very much depending on the accuracy of the solvers. For the mid-fidelity code, CIRA RAMSYS and DLR-UPM solvers underpredict the torque because they do not consider the viscosity effects in current simulation; ONERA PUMA solver approximate the viscous effects using look-up tables of the 2D-aerodynamic characteristics. The higher order of accuracy is obtained by all CFD codes except DLR TAU underestimates the value, which may be caused using full turbulence modeling or lack of grid resolution. For vortex-based methods, the choice of a vortex core model as well as a vortex core radius can influence on the inflow downwash velocity and therefore rotor thrust. For CFD-related methods, the proper choice of grid resolutions is key factor for the rotor tip vortex with less dissipation or dispersion errors. For this rotor, flow separations were observed in CFD results.

The comparison of the blade-surface pressure distribution represented as pd = p-p0 (unsteady surface pressure) among the codes is given in Fig. 9 for RPM 10000. p0 is the air pressure in undisturbed flow. The difference among the codes can be observed especially in the blade-tip region,

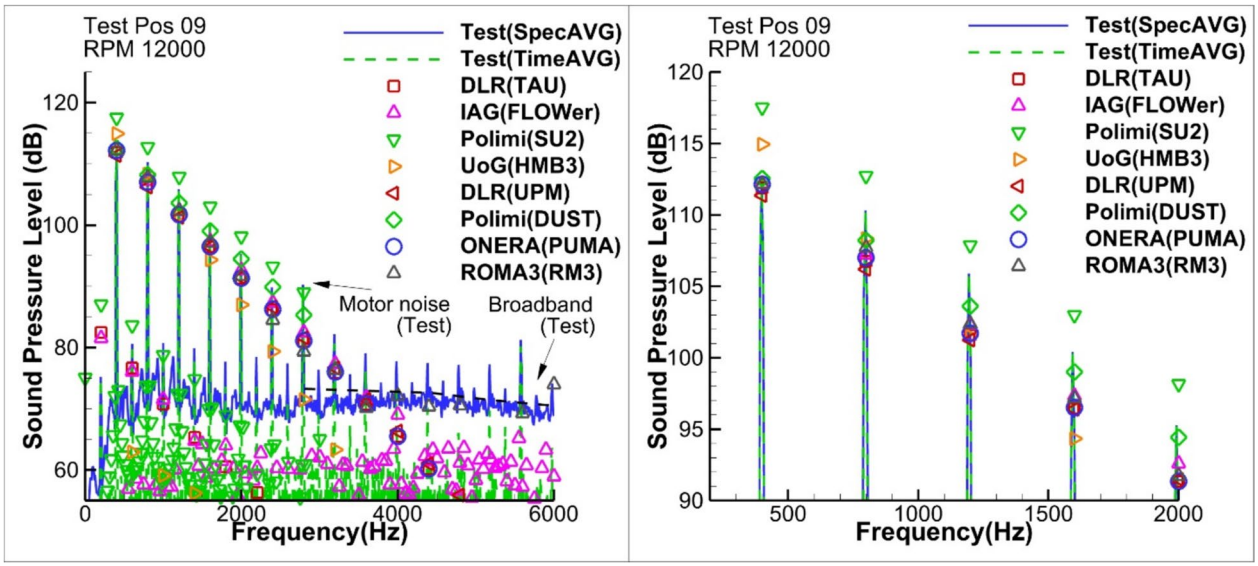

Fig. 15 Sound pressure level (SPL) spectra from the microphone located at 9 (left) and zoom view (right) for 12000 rpm

which will be reflected in the noise value. This is an instantaneous plot but the fluctuations are very low.

4.1.2 Ensemble average velocity fields

The simulated flow-field behavior is compared with ensemble average velocity fields obtained on 500 instantaneous velocity fields measured by the PIV technique [7] as shown in Fig. 10 for the isolated rotor at 10,120 rpm.

The vertical velocity-color map, together with the stream traces, provides an overview of the flow-field behavior. The mean velocity shows the typical wake contraction immediately downstream of the rotor disk. To have a quantitative comparison of PIV data, the comparisons are conducted on several slices at different Z positions marked as dashed lines in the plot. Only vertical velocity is compared.

Figure 11 shows that general forms, wake contraction, the velocity slopes in shear layer region and flow acceleration down to $z=-1$ R in the measurements are captured by most of computational tools. The comparisons are reasonably satisfactory. The PoliMi DUST results differ from other partners in positions further downstream and exhibit a small dissipation model applied in the vortex development. Possibly a too large vortex core radius was applied or the number of particles was too low.

An interesting result is obtained in terms of the shear layer region location. Indeed, all simulations predict, more or less, the same position of the shear layer, which is different from the experiment. In all simulations the radial extent of the shear layer is lower than that in the experiment. No convincing explanation is available.

The difference in the area below the rotor hub occurs mainly from the free-wake potential code results where the hub is not modeled. Therefore, root vortex from free-wake code can cause more deceleration in the flow in this area. RAMSYS and UPM results are closer to the experiment in this area. This is because the root vortex is annihilated in hover conditions. This looks like a correct modeling solution. CFD results demonstrated in general similar characteristics to other results. In addition, in ONERA, UoG and ROMA3/CNR results, as well as DLR and UoG CFD, the support strut fairing pylon is not included for the calculation, therefore significant difference occurs in the root area.

4.1.3 Aeroacoustics

The presentation of the acoustic results will focus on data taken in the test on a polar arc represented by microphones from number 5 to 11 as defined in Fig. 12. The arc is located

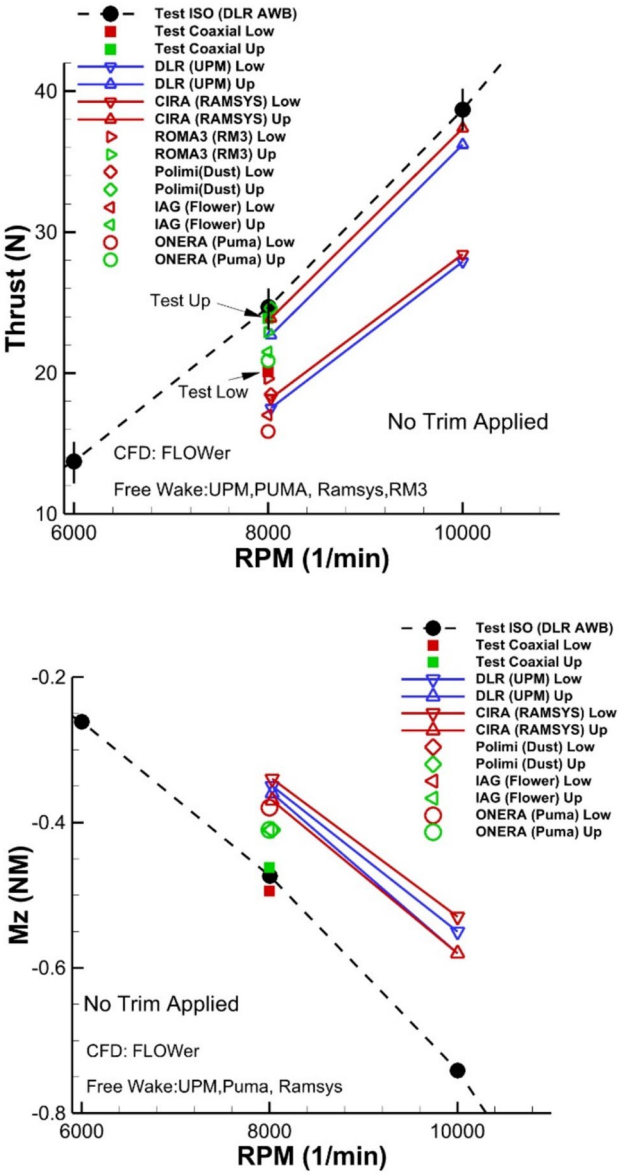

Fig. 16 Time averaged rotor thrust and torque at coaxial configuration for 10000RPM

in the Y–Z plane with an arc radius of 0.3 m and polar angle difference of 15°. The microphone 9 is located in the rotational plane (X–Y), where $Z=0$. All partners use FW-H formulation.

The polar directivities for the overall SPL derived from microphones 5 to 11 are shown for the isolated 13×7 rotor in Fig. 13. The overall sound pressure levels obtained from the test using two averaging techniques are also included. The advantage of the time-averaged noise spectrum in one rotor revolution is that the random or stochastic noise sources,

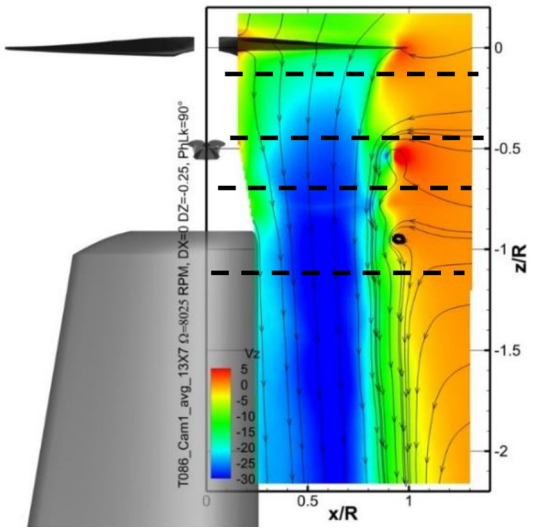

Fig. 17 Iso-contours with streamtraces of the ensemble-average flow field color-coded with the velocity vertical component for the coaxial configuration with $\Delta z = 0.5$ R at $\Omega = 8025$ RPM

such as broadband noise can be removed or reduced dramatically. For the spectrum averaging technique, the spectrum is first obtained from the time series data blocks of each rotor revolution, then averaged to obtain a mean spectrum. The comparison indicates that the acoustic simulation can capture the experimental trends for all the cases, but the numerical results for 12,000 rpm show that an averaged offset to the test results of either the time averaged or the spectrum averaged value variated between 1.1 and 3.3 dB depending on the position of the microphones. The microphone 5 is excluded in computing the averaged value as a considerable difference from test observed. The reason is that the microphone 5 located directly below the rotor, where the rotor downwash increases the microphone self-noise, which is not simulated. The higher loading noise contribution for the microphone above the rotor was predicted for all partners. In general, the contribution of the broadband noise to the Overall Sound Pressure Level, dB (OASPL) is negligible in the measurements.

There are in general an offset between the numerical results, but the noise directivity calculated by DLR, IAG and ONERA shows excellent agreement. Here the comparisons involve two fidelity levels. The agreement indicates that the wake had no significant influence as the main noise contribution came from the loading noise, which may occur for different fidelity levels. The PoliMi results are closest to the

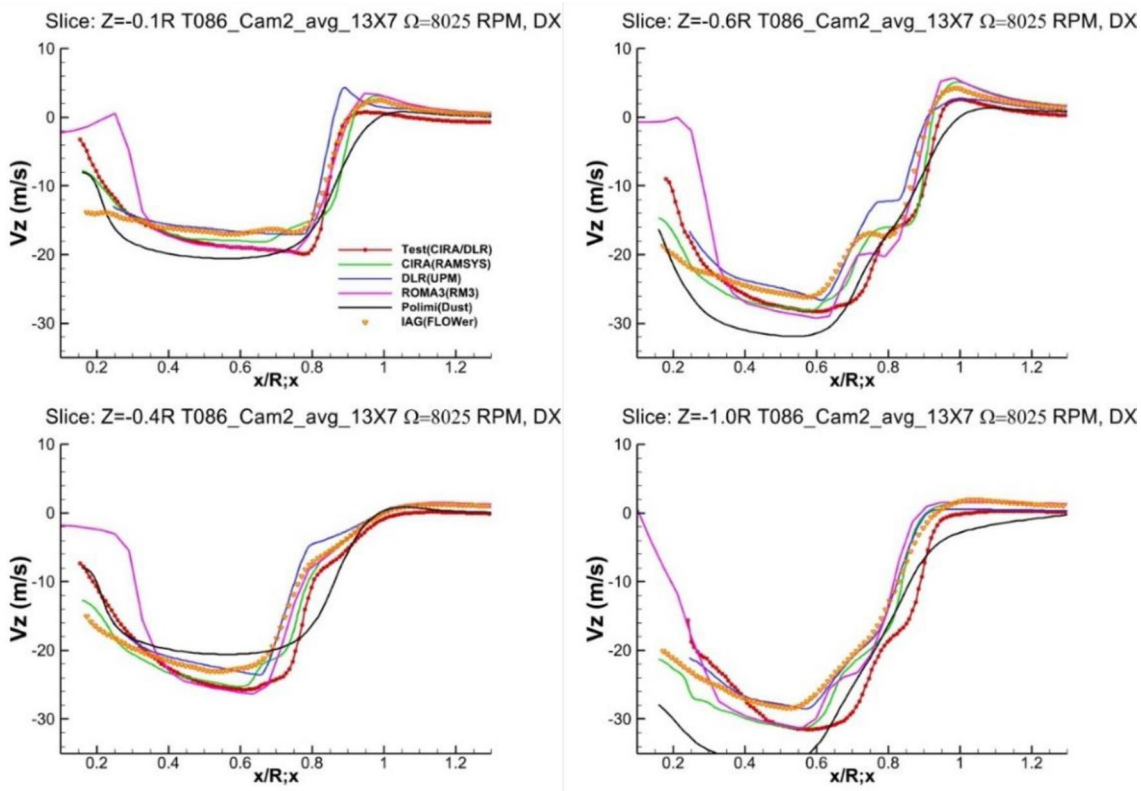

Fig. 18 Vertical velocity trend along radial distance at $\Omega = 8025$ RPM for different z-stations

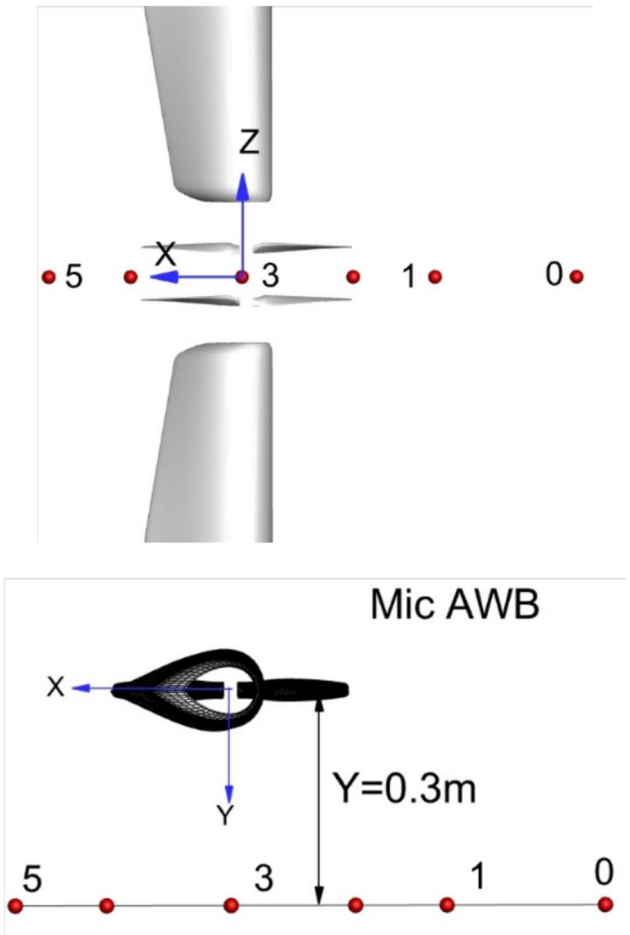

Fig. 19 Microphone positions for the coaxial rotor case

experimental data, while the results ROMA3/CNR and UoG show agreement with others. The same agreement obtains between DLR and CIRA results for RPM 10120.

A more detailed data interpretation should be based on examining the SPL spectra or the time history. The acoustic results in terms of time histories at Mic. position 9 are compared, as shown in Fig. 14. Figure 14 top compares the predicted sound pressure time history at microphone 9 for rotor thickness noise and Fig. 14 low compares overall acoustic signal. The thickness noise (monopole) and overall signal from DLR and IAG predictions are perfectly met. The difference in thickness for PoliMi already expose the possible influence of geometric discrepancy from both DLR and IAG.

The time history data from the experiment in Fig. 14 low exhibits high and low-frequency variations. The low-frequency 2-P variations are larger than the ones observed numerically, highlighting the discrepancies in thrust already observed between the test and simulations. The computations of DLR, IAG and UoG capture well the slope when the blade approaches the microphone, but mismatch the slope when the blade moves away from the microphone. The variation of the high frequency noise in the test could be attributed to the rotor broadband noise or some contamination due to reflections from the microphone support structure, etc. while the high frequency components displayed in IAG results is pure numerical artifacts.

Figure 15 compares predicted sound pressure spectra for two frequency ranges. For both the simulations and test, the rotor harmonic sound components dominate at low frequencies. Broadband noise becomes more important in the test for frequencies greater than 2 kHz, but the contribution to overall SPL can be neglected. It should be mentioned that broadband sound and motor noise contributions were not included in numerical simulations.

Figure 15 shows all numerical simulations match very well the experimental trends, in which the highest level in the spectrum is located at the first BPF and decays almost linearly with increasing frequencies. The influence of geometric difference between two blades and motor noise causes the subharmonics among the two BPFs observed in the experiment. As all CFD simulations consider the blade to blade differences, the level in subharmonics are also displayed.

5 Results two rotors in coaxial configuration

For the coaxial configuration, as shown in Figs. 2 and 5b, the distance between two rotors is defined by ΔZ/D, where D is the diameter of the rotor in 0.33 m. Both rotors are turned in opposite directions with the same rotational speed. The lower rotor, defined as rotor 1, RHR rotates counterclockwise as for the isolated condition and the upper rotor defined as rotor 2, LHR rotates clockwise. The starting phase positions of the reference blade for both rotors point toward downstream and both rotors are phase locked in the simulations. In the test however, there is no phase synchronization of the two rotors.

5.1 Hover at RPM = 8000 and Δz/D = 0.25

5.1.1 Aerodynamic performance

A comparison of the measured and simulated time-averaged rotor thrust and torque for this coaxial configuration is given in Fig. 16 together with the value from the isolated rotor. The effect of the coaxial configuration shows a slight decrement of the upper rotor thrust because of the mutual interaction with the lower rotor. An apparent effect on lower rotor for both the test and all simulations shows a more significant loss of the thrust, compared with upper rotor. This behavior is mainly due to the effect of the upper rotor downwash

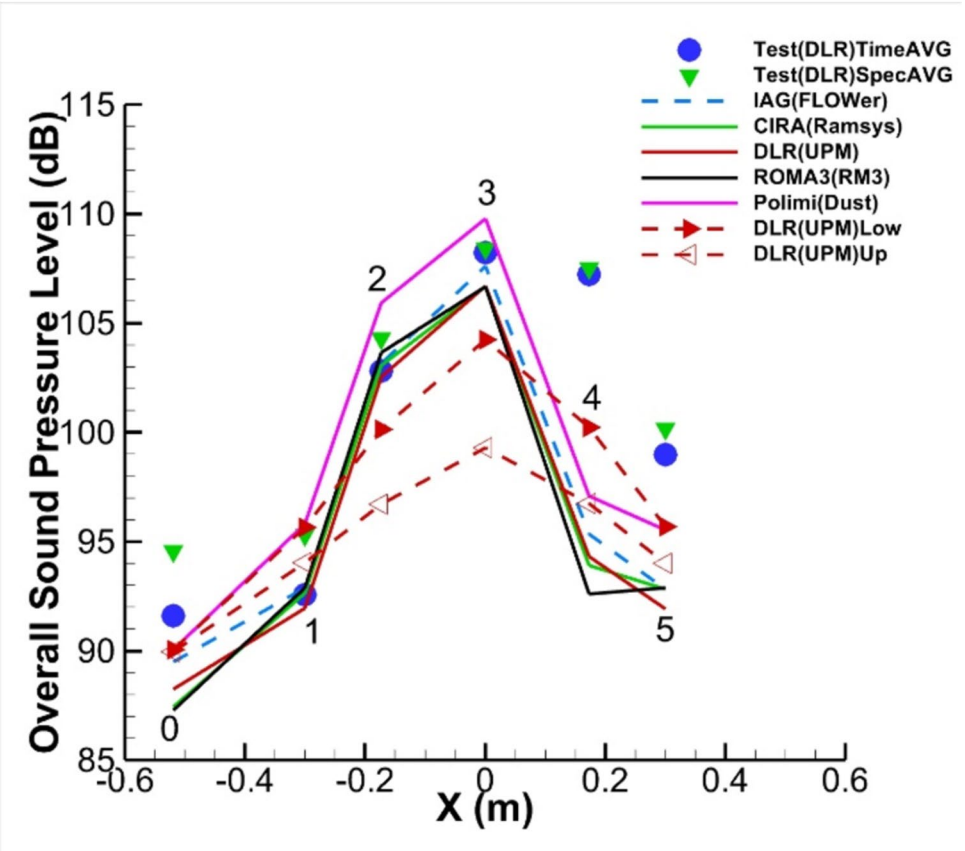

Fig. 20 OASPL directivity taken from Mic 0 to Mic 5 for RPM 8000

which increases the induced velocity and thus reduces the effective angles of attack of the lower rotor. The effect of the loss of the lower rotor thrust is captured by all codes. All simulations predict a slightly lower torque while there is almost no change of the torque in the test. CIRA and DLR conducted the predictions also for two RPM values for this configuration with very good agreements and the results indicate the general tendencies in the measurements are reproducible.

5.1.2 Ensemble average velocity fields

The ensemble average velocity fields from the measurement for the coaxial configuration with $\Delta z = 0.5$ R at $\Omega = 8025$ RPM are given in Fig. 17. As for the isolated case, the mean data are obtained by averaging a set of 500 instantaneous velocity maps. The PIV-measurement foresaw that the upper rotor was free to rotate while the lower was phase locked at rotor azimuthal position of $\Psi = 90°$ to avoid blade laser reflection in the measurement region. The mean velocity field shows the typical wake contraction downstream of the lower rotor, similar to the isolated rotor (Fig. 11).

Figure 18 depicts the comparisons on several slices at different Z positions marked as dashed lines in Fig. 17. It shows similar characteristics of the flow field demonstrated in the isolated rotor case, except in the lower slice positions, basically from z/R = − 0.5 downward, where more dynamic variations in the shear layer region are observed. Those dynamic variations are produced by the additional velocity induced by the lower propeller and are captured by all simulations with some variation in positions. IAG CFD Flower results have the same shear layer slope of the measurements but shifted and underestimate the maximum vertical velocity. CIRA and ROMA3/CNR results show shifted shear layer, but the same slope and induced velocity. DLR-UPM has similar behavior to ROMA3/CNR and CIRA but slightly underestimates the induced velocity. Low vortex dissipation is observed in PoliMi-Dust. The major discrepancies among the solvers are at the root, related to the hub modelling. For example, in CIRA RAMSYS and DLR-UPM there is no hub modelling, but numerical treatment on the root vortex.

5.1.3 Aeroacoustics

The presentation of the acoustic results will focus on data represented by microphones on a line of array from number 0 to 5 as defined in Fig. 19. The microphones are located

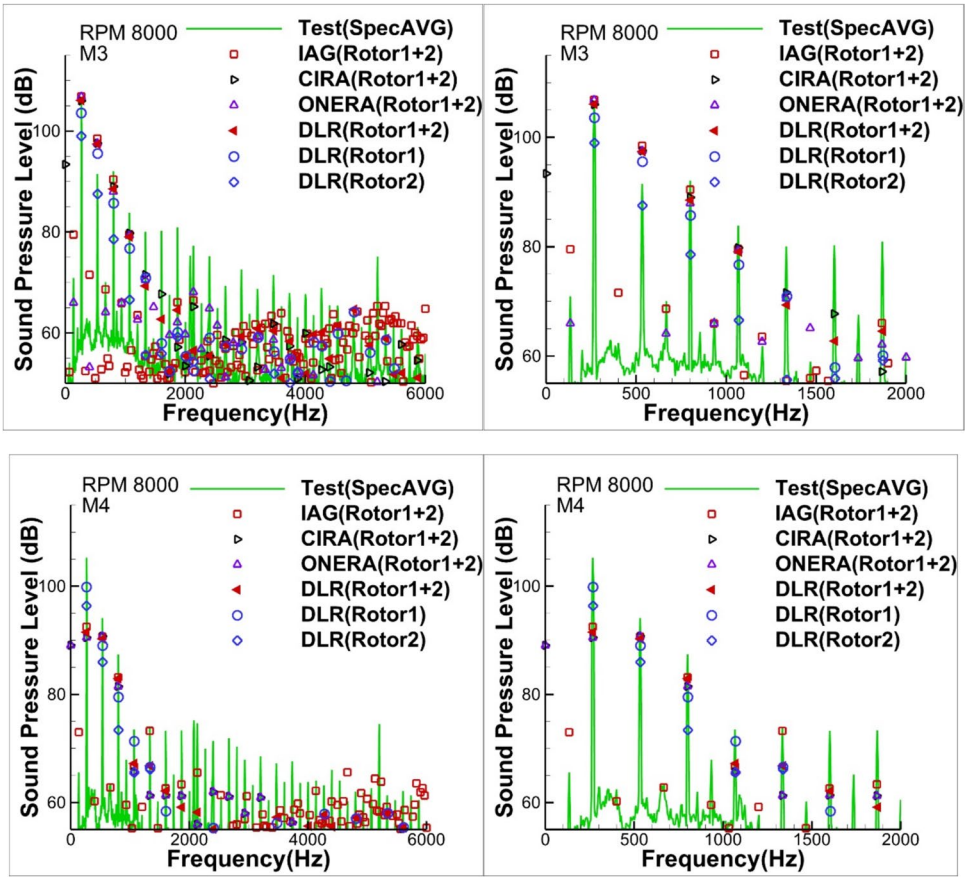

Fig. 21 Sound pressure level (SPL) spectra from the microphone located at 3 and 4 (left) and zoom view (right) for 8000 rpm

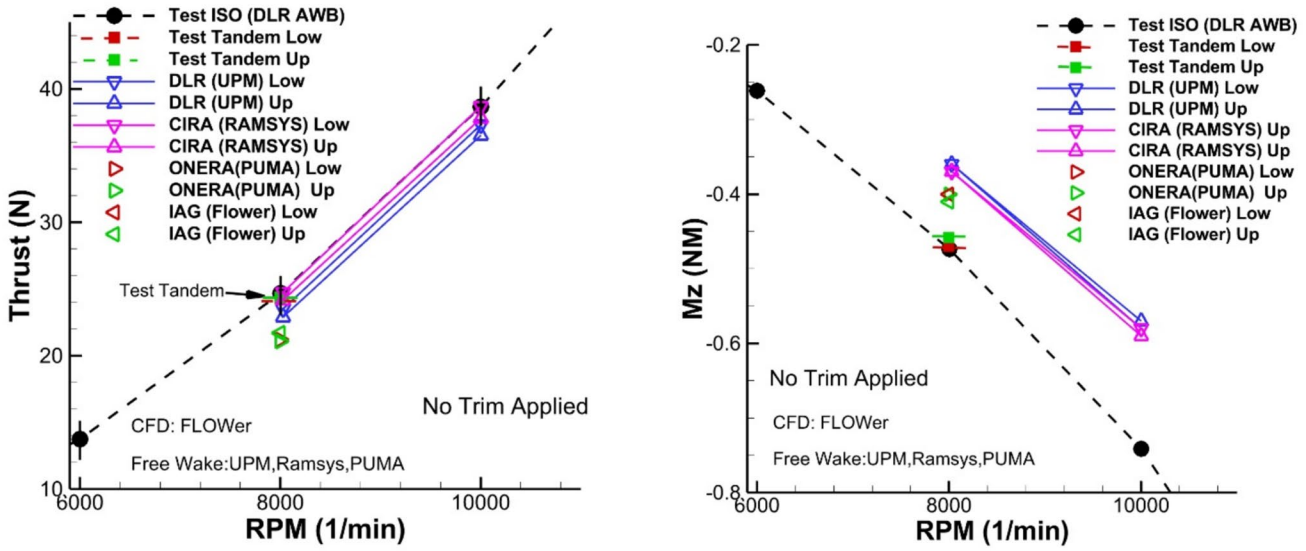

Fig. 22 Time averaged rotor thrust and torque at coaxial configuration for 10000RPM

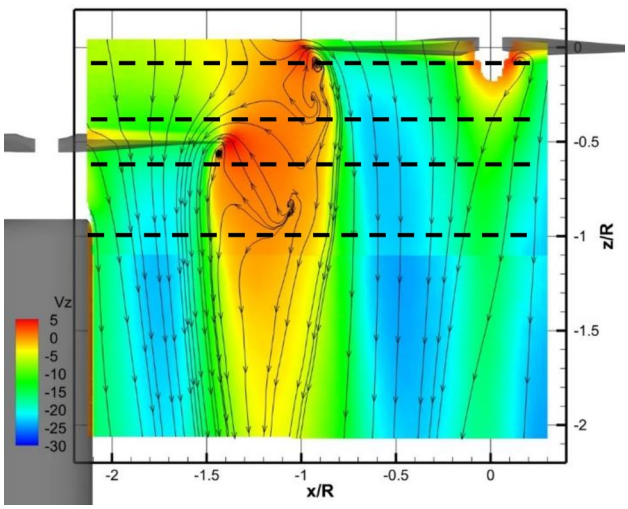

Fig. 23 Iso-contours with streamtraces of the ensemble-average flow field color-coded with the velocity vertical component for the coaxial configuration with $\Delta z = 0.5$ R at $\Omega = 8025$ RPM

in the X–Y plane with equal distance of 0.3 m to the X–Z plane.

As shown in Fig. 20, the OASPL directivity calculated by DLR, IAG, CIRA and ROMA3 shows very good agreement for all microphones although the comparisons involve two fidelity levels. PoliMi results display the highest level among the simulations. All the simulations capture the trend of the directivity. Good comparisons also observed for the microphones located at positions $X <= 0$, but large deviations from the test results for the microphones located at $X > 0$ are observed. To see the contributions from individual rotors, the individual rotor contributions from DLR simulations are also included in the plot. The noise level from lower rotor, marked as dashed red line with solid triangles is in general higher than that from the upper rotor. The higher lower rotor noise is caused possibly by higher non-uniform inflow introduced by the multi-inductions of the upper rotor wake as well as the difference in the noise directivity. When comparing the sum of the two rotor noises with the individual contributions, the acoustic interferences are well visible, indicated for example by the clear noise cancelation for the microphones located at $X > 0$. Due to the slight asynchronization of RHR and LHR in the measurement, this

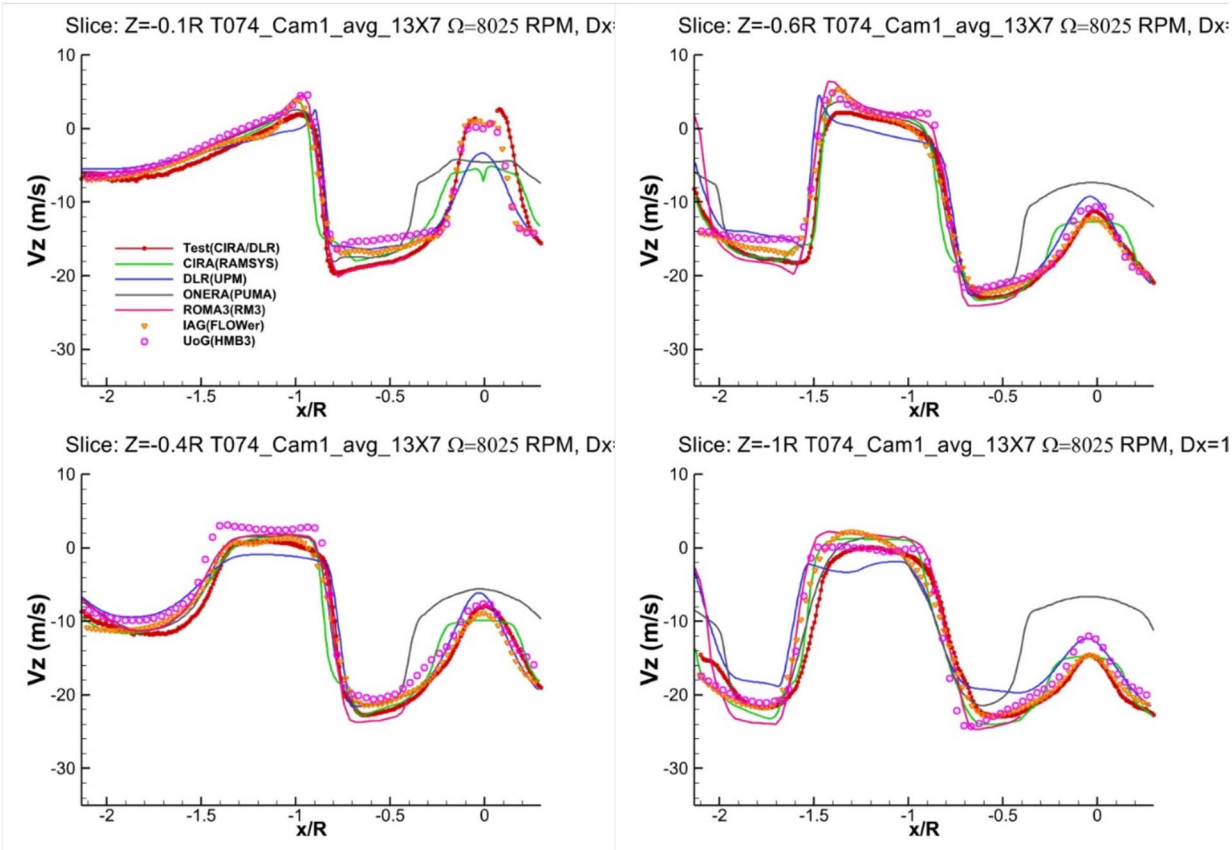

Fig. 24 Vertical velocity trend along radial distance at $\Omega = 8025$ RPM for different z-stations

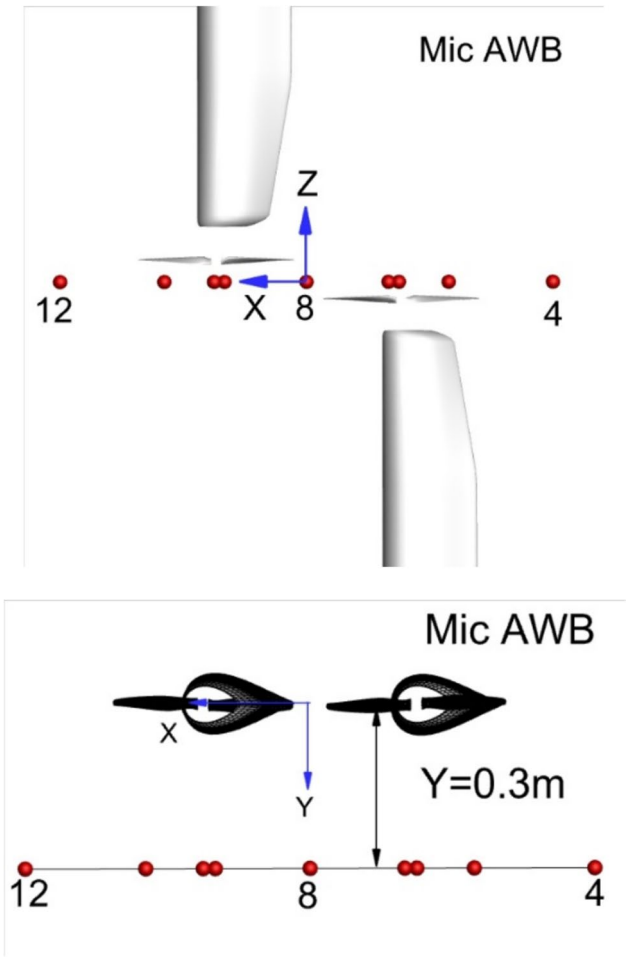

Fig. 25 Microphone positions for the tandeml rotor case

phenomenon cannot be measured, therefore large differences occur when comparing with the simulation.

Selected acoustic spectra obtained at two microphone positions (M3 and M4) are compared with the spectral-averaged test results, as shown in Fig. 21. The spectral-averaged test data are chosen to better emphasize the relative importance of both the broadband and tonal components of the source.

For the microphone located at M3, the low-frequency BPF harmonics are the dominant noise source and rotor 1 (low) noise is the dominant contributor to the SPL, according to DLR simulation. In the test results, there is an apparent increase in tonal component levels from the 3rd BPF harmonics and sub-harmonics upward. The increase in higher harmonic tonal component levels in the test may indicate more interaction related unsteadiness, primarily blade leading edge interaction, as observed in [7]. This indicates a wider part of the blade will interact with the high-intensity part of the incoming turbulent flow caused partly by the wandering of the tip vortex center. In addition, this might be an effect of the unsynchronized speed in the experiment.

For the microphone located at M4, where large deviation from the test is observed, the test result shows first BPF is the dominant tone and large difference from the numerical simulations mainly occurs for this tone. This can be partly caused by the coherent summation used by the sum of the two rotor components in the simulations. As indicated in the first BPF, the sum of the contribution of rotor 1 (low) and rotor 2 (up) causes a reduction of the overall SPL due to the coherent effect. As mentioned, this phenomenon cannot be measured due to slight asynchronization of the rotors in the measurement.

All the numerical simulations demonstrate a good agreement for the first 3 BPF tones. There is a slightly high harmonic contribution above 2000 Hz in IAG CFD results. It is possible that the simulations captured some of the high frequency contributions which can be some influence of the broadband noise, but as the broadband noise is very much related to how accuracy is the boundary lay simulation and in current simulation the focus is on the tone noise. That is reason it is cautious about assuming possible broadband contributions from IAG solver.

6 Results of two rotors in tandem configuration

For the tandem configuration, as shown in Fig. 5a, the distance between the two rotors is defined by ΔZ/D and ΔX/D, where ΔZ/D = 0.25 and ΔX/D = 1.18 are chosen. Similar to the coaxial case, the lower rotor defined as the RHR rotates count-clockwise and the upper rotor defined as LHR rotates then clockwise.

6.1 Hover at RPM = 8000 and Δz/D = 0.25 and ΔX/D = 1.18

6.1.1 Aerodynamic performance

Figure 22 compares the measured and simulated time-averaged rotor thrust and torque together with the value from the isolated rotor. The effect of this tandem configuration shows that the two rotors both in numerical simulation and in the test have very close thrust and torque values. The thrust is slightly lower than the isolated one. All codes predict a slightly high torque value. There is no apparent effect of rotor-rotor interaction as observed in the averaged performance value of the coaxial configuration.

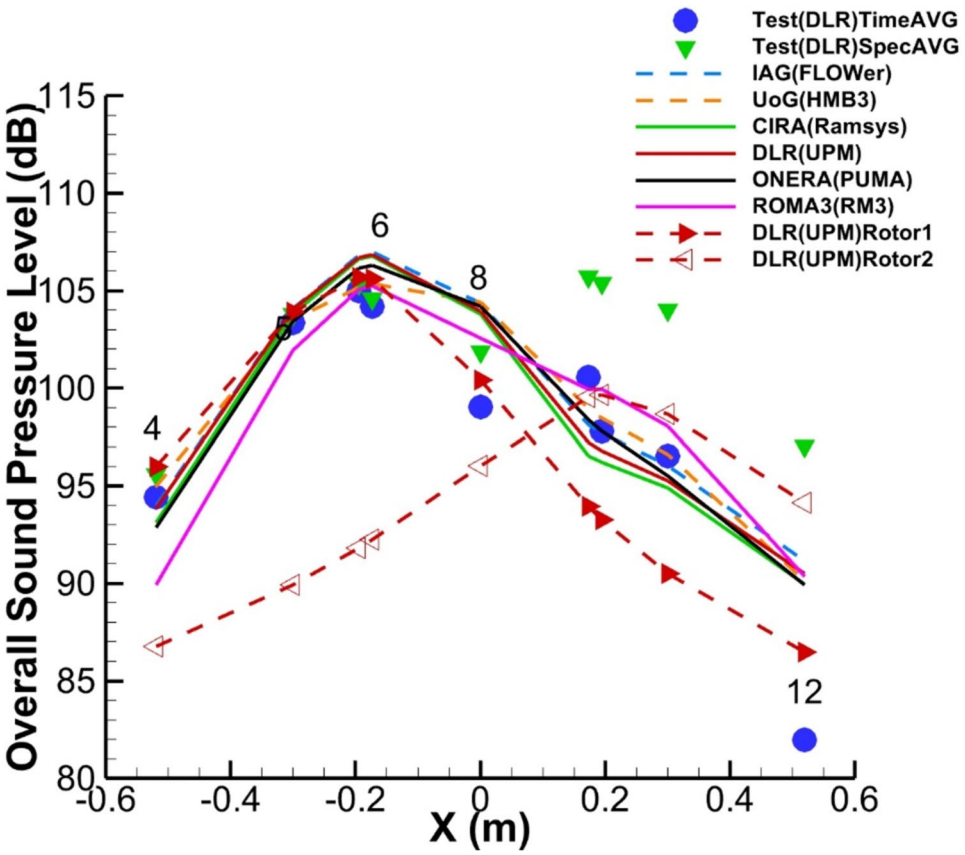

Fig. 26 OASPL directivity taken from Mic 4 to Mic 12 for RPM 8000

6.1.2 Ensemble average velocity fields

The ensemble average velocity fields from measurement for this tandem configuration at $\Omega = 8025$ RPM is given in Fig. 23. The results were obtained on 500 instantaneous velocity fields recorded avoiding any lock between the camera acquisition frequency and the rotor speed (Fig. 24).

Figure 24 compares simulated vertical velocity with the test data on several slices at different Z positions marked as dashed lines in Fig. 23. For this tandem configuration, a good agreement between simulation and experiments is obtained. The plateau showing in CIRA and ONERA results at $x/R = 0$ is related to the modelling of the rotor hub which has been explained in the previous section. The shear layer location is almost correct.

6.1.3 Aeroacoustics

Similar to the coaxial case, the acoustic results will be presented on a line of array from number 4 to 12 as defined in Fig. 25. The microphones are located in the X–Y plane with an equal distance of 0.3 m to the X–Z plane (Fig. 26).

As shown in Fig. 26, the OASPL directivity pattern fit very well among all the simulations, except ROMA3 where higher noise around rotor 2 is observed. Good comparisons with the test were also observed for the microphones located close to rotor 1 (low), except ROMA3 where lower noise around Rotor1 is observed. The deviation from the test results increases for the microphone toward rotor 2 (up). Large differences are also observed between time-averaged and spectrum averaged test results for $X > 0.2$ m, indicating possible variation of the signal within each revolution. To check the reason for the difference, the selected acoustic spectrum obtained at two microphone positions (M6 and M8) are compared with the spectral-averaged test results, as shown in Fig. 27.

For M6 and M8, the first four low-frequency BPF harmonics are the dominant source of noise. For these four BPFs, the rotor 1 (low) noise is the dominant contributor to the noise level for these selected microphones.

The large difference due to the interference effect between the simulation and test for the first BPF is observed. The interference effect may not be captured during the test.

All the numerical simulations in Fig. 27 demonstrate good agreement for the first five BPF tones.

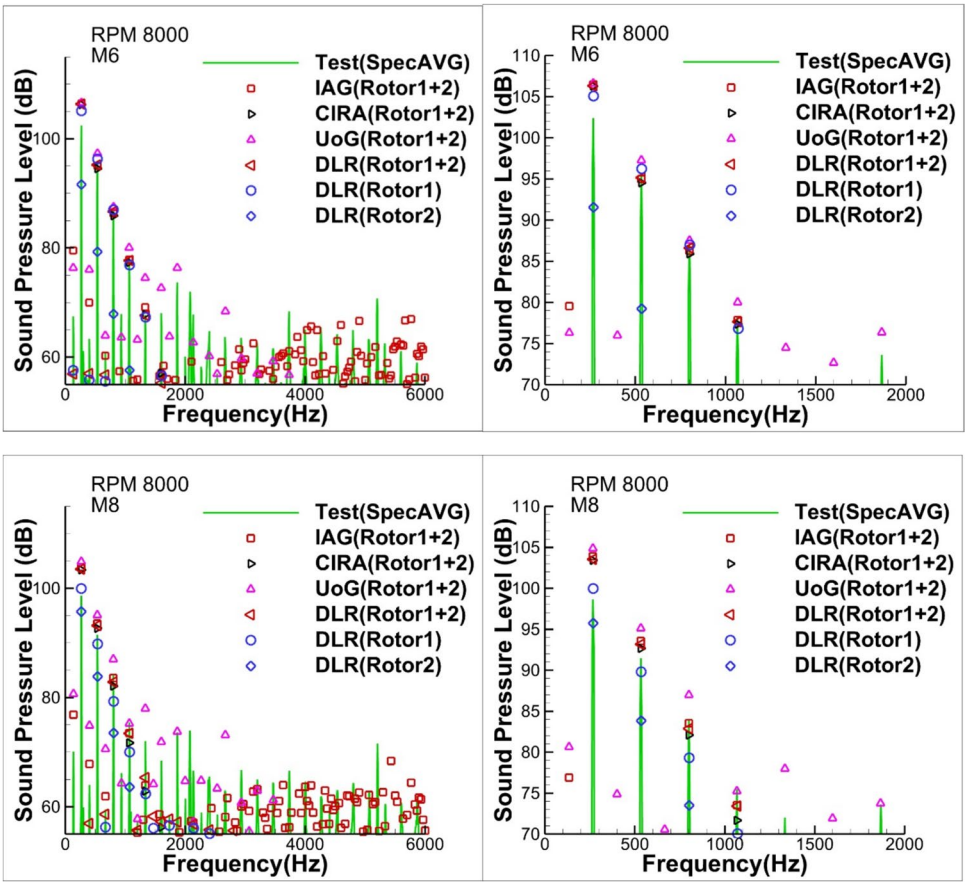

Fig. 27 Sound pressure level (SPL) spectra from the microphone located at 6 and 8 (left) and zoom view (right) for 8000 rpm

7 Conclusion

In this paper, the wind tunnel test and the numerical activities achieved in the GARTEUR AG26 are introduced. The experimental and numerical investigations of the rotors in the isolated, coaxial and tandem configurations are presented.

Comparisons of code-to-code and the code-to-test results were carried out. The test results are derived from the test carried out from CIRA/DLR PIV and DLR acoustic test. The numerical comparisons were conducted using different solvers applied by the partners within the GARTEUR Action Group AG26.

Both aerodynamic and aeroacoustic simulation indicate that measurement results in terms of rotor performance, flow field and acoustic signals for most cases were reproducible and the comparison of the simulations and the test give satisfactory agreement by all computational methods, regardless of their fidelity level. The acoustic interference can enlarge the difference in comparison with the test results in case this phenomenon is not captured in the test.

Acknowledgements The research leading to the presented results has been addressed within the framework of the HC/AG-26, supported by GARTEUR. The work of the IAG was partially supported by Bundesministerium für Wirtschaft und Technologie (BMWi) under grant agreement No. 20Q1954B as part of the Volare project.

Author contribution All authors agreed with the content and that all gave explicit consent to submit and that they obtained consent from the responsible authorities at the institute/organization where the work has been carried out, before the work is submitted.

Funding Open Access funding enabled and organized by Projekt DEAL.

Data availability No datasets were generated or analysed during the current study.

Declarations

Conflict of interest The authors declare that they have no conflict of interest.

References

1. Yin, J., De Gregorio, F., Petrosino, F., Rossignol, K-S, Schwarz, T., Cotte, B., Brouwer, H., Clero, F., Mortain, F., Reboul, G., Zanotti, A., Vigevano, L., Gibertini, G., Bernardini, G., Schmähl, M., Kaltenbach, H-K., Pagliaroli, T., Keßler, M., Barakos, G., Ragni, D., Testa, C.: Noise Radiation and Propagation for Multirotor System Configurations. In: Terms of Reference for the GARTEUR Action Group HC/AG-26. (2021)
2. Rossignol, K.-S., Yin, J., Rottmann, L.: Investigation of Small-Scale Rotor Aeroacoustic in DLR's Acoustic Wind Tunnel Braunschweig, in 28th AIAA/CEAS Aeroacoustics 2022 Conference, Southampton, UK. (2022)
3. Yin, J., Rossignol, K.-S., Rottmann, L., Schwarz, T.: Numerical Investigations on Small-scale Rotor Configurations with Validation using Acoustic Wind Tunnel Data. In: 48th European Rotorcraft Forum (ERF), 2022, Seiten 1–17. 48 European Rotorcraft Forum (ERF) 2022, Winterthur, Switzerland. (2022)
4. Nargi, R.E., Candeloro, P., De Gregorio, F., Ceglia, G., Pagliaroli, T.: Fluid-dynamic and aeroacoustic characterization of side-by-side rotor interaction. Aerospace **10**(10), 851 (2023)
5. De Gregorio, F., Candeloro, P., Ceglia, G., Pagliaroli, T.: Flow field and acoustic assessment of twin rotors in hover conditions. J. Phys. Conf. Ser. **2802**(1), 012011 (2024)
6. Zanotti, A., Algarotti, D.: Aerodynamic interaction between tandem overlapping propellers in eVTOL airplane mode flight condition. Aerosp. Sci. Technol. **124**, 107518 (2022)
7. De Gregorio, F., Rossignol, K. S., Ceglia, G., Yin, J.: Multi-rotor wake interaction characterization. 49 European Rotorcraft Forum (ERF) 2023, Bückeburg, Germany. (2023)
8. Pott-Pollenske, M., Delfs, J. W.: Enhanced capabilities of the aeroacoustic wind tunnel Braunschweig. 14th AIAA/CEAS Aeroacoustics Conference (29th AIAA Aeroacoustics Conference), 2008, AIAA-2008–2910 (2008)
9. Raffel, M., Willert, C.E., Wereley, S.T., Kompenhans, J.: Particle image velocimetry—a practical guide, 2nd edn. Springer-Verlag Berlin Heidelberg (2007). https://doi.org/10.1007/978-3-540-72308-0
10. Visingardi, A., D'Alascio, A., Pagano, A., Renzoni, P.: Validation of CIRA's rotorcraft aerodynamic modelling system with DNW experimental data. In: 22nd European Rotorcraft Forum, Brighton, UK, 1996. http://hdl.handle.net/20.500.11881/3171
11. Morino, L.: A general theory of unsteady compressible potential aerodynamics. NASA CR-2464. (1974)
12. Williams, J.E.F., Hawkings, D.L.: Sound generation by turbulence and surfaces in arbitrary motion. Philos. Trans. R. Soc. Lond. Series A Math. Phys. Sci. **264**(1151), 321–342 (1969)
13. Casalino, D.: An advanced time approach for acoustic analogy predictions. J. Sound Vib. **261**(4), 583–612 (2003). https://doi.org/10.1016/S0022-460X(02)00986-0
14. Casalino, D., Barbarino, M., Visingardi, A.: Simulation of helicopter community noise in complex urban geometry. AIAA J. **49**(8), 1614–1624 (2011). https://doi.org/10.2514/1.J050774
15. Barbarino, M., Petrosino, F., Visingardi, A.: A high-fidelity aeroacoustic simulation of a VTOL aircraft in an urban air mobility scenario. Aerosp. Sci. Technol. (2021). https://doi.org/10.1016/j.ast.2021.107104
16. Ahmed, S.R., Vidjaja, V.T.: Unsteady panel method calculation of pressure distribution on BO105 model rotor blades. J. Am. Helicopter Soc. **43**, 47–56 (1998)
17. Yin, J., Ahmed, S.R.: Helicopter main-rotor/tail-rotor interaction. J. Am. Helicopter Soc. **45**(4), 293–302 (2000)
18. Schwamborn, D., Gerhold, T., Heinrich, R.: The DLR TAU-code: recent applications in research and industry. Proceedings of European Conference on Computational Fluid Dynamics ECCOMAS CFD 2006, Delft, Netherlands. (2006)
19. Yin, J., van der Wall, B. G., Wilke, G.A.: Rotor aerodynamic and noise under influence of elastic blade motion and different fuselage modeling. 40th European Rotorcraft Forum (ERF) 2014, 2–5. Southampton, UK. (2014)
20. Mudry, M.: La théorie des nappes tourbillonnaires et ses applications à l'aérodynamique instationnaire. PhD thesis, University of Paris VI. (1982)
21. Boisard, R.: Numerical analysis of rotor/propeller aerodynamic interactions on a high-speed compound helicopter. J. Am. Helicopter Soc. **67**(1), 1–15 (2022). https://doi.org/10.4050/JAHS.67.01200
22. Cambier, L., Heib, S., Plot, S.: The ONERA elsA CFD software: input from research and feedback from industry. Mech. Ind. **14**(3), 159–174 (2013)
23. Prieur, J., Rahier, G.: Comparison of the Ffowcs Williams-Hawkings and Kirchhoff rotor noise calculations. 4th AIAA/CEAS Aeroacoustics Conference, Toulouse. (1998)
24. Rahier, G., Prieur, J.: An efficient Kirchhoff integration method for rotor noise prediction starting indifferently from subsonically or supersonically rotating meshes. 53rd AHS Annual Forum, Virginia Beach, USA. (1997)
25. Tugnoli, M., Montagnani, D., Syal, M., Droandi, G., Zanotti, A.: Mid-fidelity approach to aerodynamic simulations of unconventional VTOL aircraft configuration. Aerosp. Sci. Technol. **115**, 106804 (2021). https://doi.org/10.1016/j.ast.2021.106804
26. Economon, T.D., Palacios, F., Copeland, S.R., Lukaczyk, T.W., Alonso, J.J.: SU2 an open-source suite for multiphysicsì simulation and design. AIAA J. **54**(3), 828–846 (2016). https://doi.org/10.2514/1.J053813
27. Galimberti, L., Morelli, M., Guardone, A., Zhou, B.Y.: Propeller noise prediction capabilities within SU2. Proceedings of the AIAA SCITECH 2023 Forum, National Harbor, MD & Online. p. 1548. https://doi.org/10.2514/6.2023-1548. (2023)
28. Gennaretti, M., Bernardini, G., Serafini, J., Romani, G.: Rotorcraft comprehensive code assessment for blade–vortex interaction conditions. Aerosp. Sci. Technol. **80**, 232–246 (2018)
29. Gennaretti, M., Colella, M.M., Bernardini, G.: Prediction of tiltrotor vibratory loads with inclusion of wing-proprotor aerodynamic interaction. J. Aircr. **47**(1), 71–79 (2010)
30. Leone, S., Testa, C., Greco, L., Salvatore, F.: Computational analysis of self-pitching propellers performance in open water. Ocean Eng. **64**, 122–134 (2013)
31. Gennaretti M., Iemma U., Testa, C.: Prediction of sound scattered by moving bodies with applications to propeller-driven airplanes. 12th AIAA/CEAS Aeroacoustics Conference. **2**, 969–980. https://doi.org/10.2514/6.2006-2475 (2006)
32. Testa, C., Greco, L., Bosschers, J.: Marine propeller shaft loading analysis in moderate oblique-flow conditions. Ocean Eng. (2022). https://doi.org/10.1016/j.oceaneng.2022.112199
33. Greco, L., Testa, C., Salvatore, F.: Design oriented aerodynamic modelling of wind turbine performance. J. Phys. Conf. Ser. **75**(1), 012011 (2007). https://doi.org/10.1088/1742-6596/75/1/012011
34. Gennaretti, M., Bernardini, G.: Novel boundary integral formulation for blade-vortex interaction aerodynamics of helicopter rotors. AIAA J. **45**(6), 1169–1176 (2007)
35. Farassat, F.: "Derivation of Formulations 1 and 1A of Farassat," Tech. Rep. NASA/TM—2007-214853, National Aeronautics and Space Administration, Langley Research Center, Hampton, VA, March 2007

36. Kroll, N., Rossow, C. C., Becker, K., Thiele, F.: MEGAFLOW-a numerical flow simulation system,} 21st ICAS congress, Melbourne, Austrila, Sep. pp. 09–13. (1998)
37. Keßler, M., Frey, F., Letzgus, J., Ohrle, C., Thiemeier, J., Krämer, E.: Progress in IAG's rotorcraft simulation framework, high performance computing in science and engineering '20, Springer International Publishing. pp. 331--341. ISBN: 978-3-030-80602-6 (2021)
38. Keßler, M., Wagner, S.: Source-time dominant aeroacoustics. Comput. Fluids **33**, 791–800 (2004)
39. Jameson, A.: Time dependent calculations using multigrid, with applications to unsteady flows past airfoils and wings, AIAA 10th Computational Fluid Dynamics Conference, Honolulu, Hawaii. (1991). https://doi.org/10.2514/6.1991-1596
40. Borges, R., Carmona, M., Costa, B., Don, W.S.: An improved weighted essentially non-oscillatory scheme for hyperbolic conservation laws. J. Comput. Phys. **227**(6), 3191–3211 (2008). https://doi.org/10.1016/j.jcp.2008.11.038
41. Steijl, R., Barakos, G., Badcock, K.: A framework for CFD analysis of helicopter rotors in hover and forward flight. Int. J. Numer. Meth. Fluids **51**(8), 819–847 (2006)
42. Biava, M., Woodgate, M., Barakos, G.N.: Fully implicit discrete adjoint methods for rotorcraft applications. AIAA J. **54**(2), 735–749 (2016)
43. Antoniadis, A., Drikakis, D., Zhong, B., Barakos, G., Steijl, R., Biava, M., Vigevano, L., Brocklehurst, A., Boelens, O., Dietz, M., et al.: Assessment of CFD methods against experimental flow measurements for helicopter flows. Aerosp. Sci. Technol. **19**(1), 86–100 (2012)
44. Steininger, R., Barakos, G. N., Woodgate, M. A.: Numerical analysis of HVAB and STAR rotor blades using HMB3. AIAA SCITECH 2023 Forum. p. 1189. (2023)
45. Babu, S., Loupy, G., Dehaeze, F., Barakos, G., Taylor, N.: Aeroelastic simulations of stores in weapon bays using Detached-Eddy Simulation. J. Fluids Struct. **66**, 207–228 (2016). https://doi.org/10.1016/j.jfluidstructs.2016.07.014
46. Barakos, G., Johnson, C.: Acoustic comparison of propellers. Int. J. Aeroacoust. **15**(6–7), 575–594 (2016). https://doi.org/10.1177/1475472X16659214
47. Qiao, G.: Parametric study of aerodynamic performance of equivalent ducted/un-ducted propellers based on high-fidelity computational fluid dynamics, Master's thesis, University of Glasgow. http://theses.gla.ac.uk/id/eprint/82702. (2021)
48. Menter, F.R.: Two-equation eddy-viscosity turbulence models for engineering applications. AIAA J. **32**(8), 1598–1605 (1994)
49. Smith, D., Filippone, A., Barakos, G.: Acoustic analysis of counterrotating open rotors with a locked blade row. AIAA J. **58**(10), 4401–4414 (2020)
50. Qiao, G., Zhang, T., Barakos, G.: Numerical simulation of distributed propulsion systems using CFD. Aerosp. Sci. Technol. (2024). https://doi.org/10.1016/j.ast.2024.109011
51. Qiao, G., San Martin, E., & Barakos, G.: Assessment of synchrophasing for a pair of rotors in close proximity. Available at SSRN https://doi.org/10.2139/ssrn.4811595